Geomechanical behaviour of heterogeneous laboratory carbonate faults

Implications for induced seismicity in geothermal reservoirs

AESM7000: Master Thesis

Jip van Dijk

Delft University of Technology

TU Delft

Geomechanical behaviour of heterogeneous laboratory carbonate faults

Implications for induced seismicity in geothermal reservoirs

by

Jip van Dijk

to obtain the degree of Master of Science

at the Delft University of Technology,

to be defended publicly on Tuesday 22 july, 2025 at 15:30.

Student number:	5180554	
Project duration:	November 11, 2024 – July 22, 2025	
Thesis committee:	Dr. Anne M.H. Pluymakers	TU Delft, Main supervisor
	Prof. Dr. P.J. Vardon	TU Delft, Assessment Committee
	Ir. Entela Kane	TU Delft, Daily supervisor

An electronic version of this thesis is available at http://repository.tudelft.nl/.

TU Delft

Preface

First of all, I would like to thank my supervisor, Entela Kane, for the help and support during this master's thesis for both thesis and non-thesis related topics. Helping with weekly meetings, questions, laboratory support and feedback through the project. I would also like to thank Anne Pluymakers for the assistance during the project and for structuring the discussion part towards the end. I want to thank Phil Vardon for serving as a member of the thesis committee. Additionally, I would like to thank Milad for his help and explanations on both displacement and injection-driven experiments.

I would also like to thank Marc and the rest of the technical staff for their support in the laboratory. Their help was invaluable during both the sample preparation and testing phases of the thesis. I would also like to thank Andre Niemeijer for allowing me to use the profilometer at Utrecht University, which helped me capture the roughness of my samples.

Additionally, I would like to thank my friends and roommates who helped me have a wonderful time in Delft over the past two years. I also want to thank my taxi drivers, who have brought me to and picked me up from the train station every Monday morning and Friday evening, and supported me over the past two years.

Jip van Dijk
Delft, July 2025

Summary

This thesis examines the geomechanical behaviour of heterogeneous carbonate rocks under laboratory conditions, with a focus on how contrast in lithologies influences fault reactivation and implications for induced seismicity in geothermal reservoirs. As there is significant geothermal potential in carbonate reservoirs in north-western Europe, geothermal energy extraction will be crucial for the energy transition. However, human interference with the subsurface is never without risks. In the past, numerous seismic events have been associated with subsurface activities in carbonate rocks. To better understand these risks, laboratory setups can be used to study these effects on a smaller scale.

We utilised two distinct carbonate rocks in this thesis: the Dinantian carbonate (lower porosity) and Indiana limestone (higher porosity). We tested these intact rocks in a series of uniaxial and triaxial compression experiments to characterise the rock properties mechanically. From these rocks, we created laboratory faults at an angle of 35° for each lithology and a heterogeneous configuration where the lithologies were mixed. In our displacement-driven experiments, we investigated the impact of surface roughness and juxtaposition of the mixed configurations. For the injection-driven experiments, only one kind of roughness is investigated, along with juxtaposition and pore pressure on fault stability.

The results on intact rocks in both confined and unconfined conditions learned us that the stiffness of Dinantian carbonate samples is the highest among all the samples. Hence, the matrix itself accommodates minimal deformation until failure occurs, either through the development of a shear fracture under confined conditions or via axial splitting in UCS tests. For the Indiana limestone, we observed a more compliant behaviour characterised by strain hardening and compaction under confined conditions. In the displacement-driven experiments, this translated into the highest critical Mohr-Coulomb stresses for the Dinantian carbonate, independent of roughness. Dependent on the type of roughness, either the Indiana limestone or the mixed samples with increased roughness exhibited the lowest critical Mohr-Coulomb stresses. The results indicated that the reactivation stresses tend towards the more compliant lithology in a heterogeneous configuration. In our injection-driven experiments, we observed an opposite trend where reactivation in the Dinantian carbonate tends to reactivate with significantly less pore pressure compared to the Indiana limestone and the heterogeneous configurations. This results from the difference in fracture flow in the Dinantian carbonate versus matrix flow in the Indiana limestone. Fracture flow results in a local distribution of pore pressure, which causes early reactivation compared to the more equal distribution along the fault in the Indiana limestone. In heterogeneous configurations, we observed again a behaviour that tends towards the compliant lithology, as the pore pressure can distribute evenly over the sample in the Indiana limestone part.

This implies that induced seismicity appears to be a higher risk in a critically stressed fault zone with less porous carbonate rocks that exhibit secondary permeability in the form of fractures.

Contents

1

Introduction

1.1. Energy transition

In 2015, 196 countries agreed upon the Paris Agreement, committing to ambitious climate action to mitigate greenhouse gas emissions to limit the rise in average global temperatures to well below 2°C above pre-industrial levels (UNFCCC, 2015). This collective effort highlights the international awareness of the need for measures to address climate change and secure a more sustainable energy source in the future.

Historically, the subsurface has been important in energy extraction, serving as a primary source of hydrocarbons (Gardiner et al., 2023). The role of the subsurface in the energy domain is expected to continue in the energy transition (Figure 1.1). Geoenergy solutions such as geoenergy exploitation and storage (ie. geothermal energy, hydrogen storage and Carbon Capture and Storage) will be needed to reach net-zero emissions (International Energy Agency, 2024).

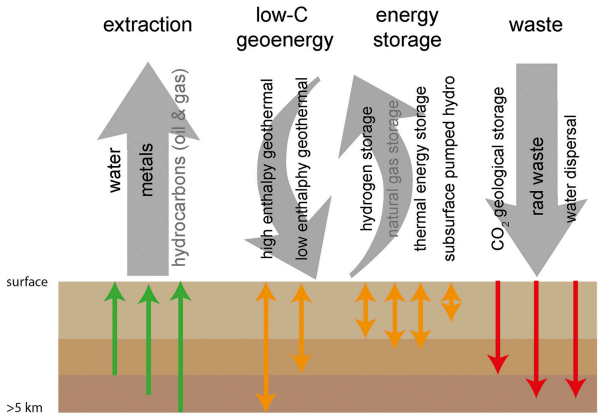

Figure 1.1: Role of the subsurface in energy transition (P. J. Cook, 2017)

Therefore, the use of geothermal energy can be of great importance in the coming years. Generally speaking, there are 3 different types of geothermal energy, characterised by depth (Masterplan, 2018).

- Heat and Cold Storage in Shallow Aquifers: This category includes systems such as Aquifer Thermal Energy Storage (ATES) and borehole heat exchangers, typically operating at depths of up to 500 meters. ATES systems are designed to address the seasonal mismatch in energy demand, particularly in temperate climates where there is an excess of heat during summer and a significant heat deficit in winter. This technology is now widely adopted for urban building applications (Bloemendal, Olsthoorn, and Ven, 2015; Bloemendal, Jaxa-Rozen, and Olsthoorn, 2018).

- Deep Geothermal Energy: This involves extracting hot water from underground layers at depths ranging from 500 meters to 4 kilometres. Within the Netherlands, the thermal gradient is around 30°C/ km (Bonté, Van Wees, and Verweij, 2012). Therefore, the extraction of geothermal energy at lower depths will require the use of a heat exchanger. At greater depths, between 2 and 3 kilometres, temperatures range from 60°C to 90°C and are suitable for direct heating.
- Ultra-Deep Geothermal (UDG): Utilises the extraction of brine at depths greater than 4 km. Here temperatures are well above 120 °and have high enthalpy with the potential to generate electricity (Boxem et al., 2015).

Figure 1.2 illustrates different types of geothermal systems related to these depths. As shown, geothermal energy occurs in many different forms, depending on the regional geology and tectonic setting (Buijze et al., 2019).

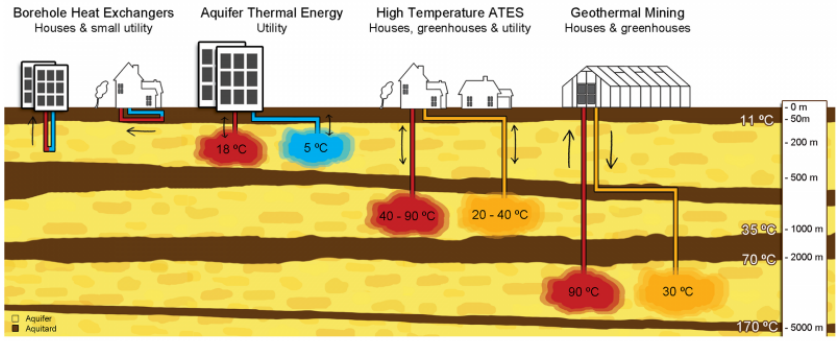

Figure 1.2: Overview of different type of geothermal systems (Vardon et al., 2025)

In addition to classification based on depth, geothermal systems can also be categorised by type (Breede, Dzebisashvili, and Falcone, 2015). They identified several types, with the most relevant ones described below:

- Hydrothermal systems (HS): These are geothermal fields associated with active convection-dominated systems. In such systems, temperatures exceeding 200 °C can be accessed at relatively shallow depths of up to 3 km. The natural permeability in these systems is sufficiently high to allow for energy production without the need for stimulation.
- Petrothermal systems (PS): These systems target formations with low natural permeability, requiring stimulation to enhance it. Petrothermal systems are also referred to as Enhanced Geothermal Systems (EGS), where the injection pressure is very high to increase the permeability in a reservoir by utilising fracture networks(Buijze et al., 2019).
- Hot sedimentary aquifers (HSA): These involve extracting geothermal energy from porous sedimentary rock formations. In the Netherlands, these formations are typically found at depths ranging from 1.5 to 3 km, with temperatures reaching up to 100 °C (Buijze et al., 2019).

Within the Netherlands, 33% of CO_2 emissions stem from the heating and electricity sector (International Energy Agency (IEA), 2025), and 11% of CO_2 emissions are from residential sources. Hence, utilising the heat extracted from geothermal fluids can assist in decarbonising the heating of households, within the greater frame of increasing the capacity from 6.9 TJ to 15 PJ of geothermal energy in 2030 and 200 PJ in 2050 (Ministerie van Klimaat en Groene Groei, 2023; Rijksoverheid, 2019; Masterplan, 2018). Currently, the contribution of geothermal energy is only 0.0009% to the total heat production in the Netherlands (Ministerie van Klimaat en Groene Groei, 2023; Energie Beheer Nederland, 2025). The aim is to increase by over 20% (Masterplan, 2018), therefore, the number of geothermal doublets in the Netherlands must increase significantly. As of 2023, only 20 doublets were operational, but

reaching the desired targets will require this number to grow into the hundreds (Buijze et al., 2019; Ministerie van Klimaat en Groene Groei, 2023).

When broadening the scope of geothermal energy exploitation to North-Western Europe, and specifically for Germany, the United Kingdom, Belgium, and France, it becomes evident that significant progress can also be achieved in reducing CO_2 emissions. In 2022, between 13% and 39% of the annual CO_2 emissions of these countries were attributed to heating and electricity production (International Energy Agency (IEA), 2025). Interestingly, geothermal energy production is already more developed in some of these countries than in the Netherlands. For instance, Belgium reports an annual geothermal heat production of 67 TJ, while Germany and France produce 3,021 TJ and 6,302 TJ, respectively, in 2023 (International Energy Agency (IEA), 2025). These numbers highlight the potential for further upscaling geothermal energy production across the Dutch domain.

1.2. Ultra-deep Geothermal targets in North-West Europe

Carbonate rocks represent some of the most promising geothermal reservoirs, owing to their potential for high fluid flow through fractures and/or karsts. Additionally, their capacity to retain high enthalpy makes them well-suited for efficient geothermal energy production (Montanari et al., 2017).

In North-West Europe, there is significant interest in the development of Ultra-Deep Geothermal systems. This interest comes from the potential to generate electricity, as high-enthalpy systems are capable of generating electricity (Boxem et al., 2015). A potential target for that is the Lower Carboniferous Dinantian carbonate formation. Geothermal projects in the Netherlands and Belgium have already explored and exploited carbonate reservoirs within the Dinantian Formation at shallower depths, providing valuable analogues (Buijze et al., 2019; Broothaers et al., 2021). However, other carbonate formations produce geothermal energy in Germany and France (Seithel et al., 2019; Lopez et al., 2010).

1.3. Geology of carbonate rocks

To gain a better understanding of carbonate rocks, it is necessary to examine their geological characteristics. The geological characteristics of carbonate rocks refer to their chemical composition, grain size, texture, type of porosity and permeability (Chilingar, Bissell, and Fairbridge, 2011). Based on the aforementioned characteristics, various classification schemes have been proposed in the literature. In this study, we will primarily focus on texture-based classification, as it provides a relatively straightforward approach to distinguishing carbonate rocks. Additionally, we will briefly discuss classifications based on porosity and permeability.

Carbonate rocks predominantly occur in the following chemical types: calcium carbonate ($CaCO_3$), calcium magnesium carbonate ($CaMg(CO_3)_2$) or siderite ($FeCO_3$). These are mostly formed through deposition in marine environments from biological or chemical processes (diagenesis). Limestones can also form in deep-water zones or within coral atoll formations (Chilingar, Bissell, and Fairbridge, 2011).

In 1962, Dunham proposed a classification system to describe carbonate rocks, based on their depositional texture. Both mudstones and wackestones are mud-supported but differ in the proportion of grains they contain. Packstones, while containing mud, are grain-supported, whereas grainstones are entirely grain-supported. The progression from mudstones to grainstones reflects an increase in the energy of the depositional environment (Dunham, 1962). Figure 1.3 provides a visual representation of this classification. Additionally, the classification includes boundstones, formed through binding processes during deposition. For recrystallised carbonates, the original depositional characteristics are not very clear due to recrystallisation.

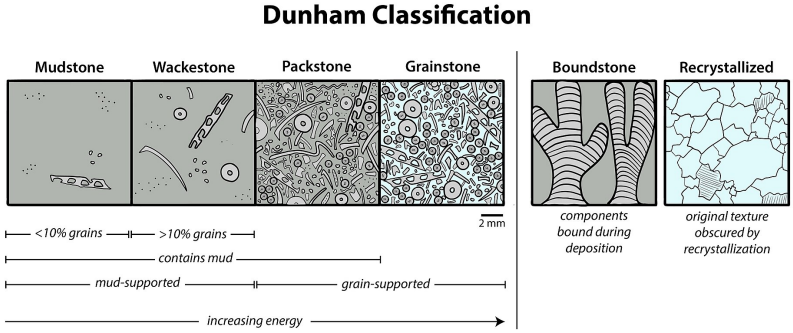

Figure 1.3: Overview Dunham classification of carbonate rocks (Quinton, 2025; Dunham, 1962)

In addition to the Dunham classification of carbonate types, alternative frameworks have been developed to describe carbonate porosity. In 1952, Archie introduced a classification system based on matrix porosity (Archie, 1952). Similarly, Lucia proposed a system focusing on the relationship between porosity and carbonates (Lucia, 1983). However, the classification developed by Choquette and Pray remains the most widely adopted in geosciences. This framework is particularly favoured due to its applicability to geological models incorporating depositional environments and subsequent diagenetic processes (Moore and Wade, 2013). Within carbonate rocks, porosity and permeability are influenced by three primary mechanisms: depositional processes, diagenetic alterations, and fracturing (Ahr, 2011). As a result of these processes, porosity and permeability are affected, with direct implications on the geomechanical behaviour of carbonate rocks.

1.4. Geomechanical behaviour of carbonate rocks and faults

The geological characteristics of carbonate rocks (ie. chemical composition, grain size, texture, porosity type and permeability) directly impact the mechanical properties of carbonate rocks (Perras and Diederichs, 2011). Among the aforementioned properties, the focus is on the effect of rock chemistry and porosity on the geomechanical behaviour of carbonate rocks.

The chemical composition of the carbonate rocks plays an important role in their triaxial strength, as variations in mineralogical composition can further affect the mechanical performance (Abd El-Aal et al., 2021). The literature indicates, for instance, that the triaxial strength of a low porous calcium–magnesium carbonate (dolomite) is greater than that of a low porous calcium carbonate (limestone) (Lin et al., 2021).

Higher porosity typically results in lower strength, as the increased void space reduces the material's ability to withstand applied loads (Přikryl, 2001). This trend is also documented for carbonate rocks (Zhu, Baud, and Wong, 2010). Consequently, the presence of fluids can dissolve carbonate minerals, increasing porosity and subsequently altering the rock's mechanical properties (Kortram, Barnhoorn, and A. Pluymakers, 2023).

Natural fault zones consist of areas with high and low deformation zones, referred to as the fault core and damage zone, respectively (Torabi, Johannessen, and Tor Saltnes Skram Ellingsen, 2019; Caine, Evans, and Forster, 1996; Childs et al., 2009; C. A. J. Wibberley, Yielding, and Di Toro, 2008). The fault core accommodates most of the displacement and strain in the fault zone. The damage zone is characterised by a wide range of fractures and faults, with deformation bands depending on the porosity of the rock (Torabi, T. Ellingsen, et al., 2019; Faulkner et al., 2010; Rotevatn et al., 2016). The spatial scale of both the damage zone and fault core reflects the temporal evolution of the fault.

A fault may begin to develop once the mechanical threshold of a particular layer is exceeded. This process can occur within a sequence of alternating relatively brittle and less brittle layers. For example, in a sequence of limestones and shales, brittle deformation may initiate in the limestone through the formation of veins or fractures, which create a weaker zone. In contrast, the shale layers accommodate this deformation through ductile extension, without fracturing. This extension can continue into shear-

ing as deformation progresses (DCP Peacock and Sanderson, 1992; D.C.P Peacock, 2002). Fault propagation will preferentially occur in the direction of the minimum principal stress.

In carbonate fault zones, a complex interplay of structural, mechanical, and chemical processes controls fault behaviour. Consequently, the geomechanical response of these zones is highly influenced by host rock, damage zone, fault core, fault roughness and fluid properties. These include host rock porosity, permeability, lithology, fluid presence, and fault maturity (Delle Piane et al., 2017).

In low-porosity carbonate rocks, outcrop-scale deformation is predominantly brittle and localised depending on the geometry of the fault offset (Bastesen and Braathen, 2010). The well-defined fault core is composed of cataclastic gouge and slip zones, with a typically broader damage zone with fractured host rocks. The zone can also feature calcite-filled veins, slicken lines, or polished slip surfaces, which indicate fluid involvement and repeated fault activity (Agosta and Kirschner, 2003; Bussolotto et al., 2007). At the microscale, deformation can occur in the form of ductile recrystallisation in combination with brittle mechanics. This becomes clear by the existence of veins, intergranular cracks and brecciation (Delle Piane et al., 2017).

In porous carbonate rocks, outcrop-scale deformation is primarily controlled by non-dilatant, brittle processes such as compaction and cataclastic deformation bands, which reduce porosity and grain size (Delle Piane et al., 2017; Rotevatn et al., 2016). Therefore, fault cores can have a small grain size, measuring tens of centimetres in length. With one both side slip surface where displacement is localised. The existence and continuity of the core depend on the amount of displacement. The damage zone can be recognised by minor faults and fractures characterised by shear strike-parallel to fault strike (Micarelli, Benedicto, and C. Wibberley, 2006). At the microscale, deformation occurs through brittle mechanisms, such as pore collapse, grain rotation, sliding, and fracturing, with minor ductile contributions (Cilona et al., 2012).

In literature, fault roughness is widely described as a key parameter influencing fault strength and stability (Aki, 1984; Okubo and Dieterich, 1984; Power, Tullis, and Weeks, 1988). The interaction between fault asperities plays a significant role in the reactivation of fault surfaces. Observations from outcrops further indicate that, as faults mature, their surface tends to become smooth. Moreover, fault surfaces are generally softer in the slip-parallel direction than in the slip-perpendicular direction (Sagy, Brodsky, and Axen, 2007; Candela et al., 2012).

1.5. Induced seismicity in carbonate reservoirs

Human interference in the subsurface for geoenergy or geostorage purposes perturbs the stresses, and hence the system may destabilise and potentially create seismic slip, also known as induced seismicity. Numerous seismic events have been associated with subsurface activities (Buijze et al., 2019; Ellsworth, 2013).

Fault reactivation occurs from changes in in-situ stresses that are normal and/or tangent to the fault, pore pressure perturbation, and chemical and temperature effects. The criteria for fault reactivation can be assessed using the Mohr-Coulomb failure envelope. However, seismicity only occurs if the slip becomes unstable following reactivation. Whether the slip is stable or unstable can be determined using the Rate and State friction parameters (Dieterich, 1979; Ruina, 1983).

Around the world, there are multiple examples of induced seismicity in carbonate rock reservoirs. In 2013, a magnitude 4.1 earthquake occurred as a result of an underground natural gas storage project in offshore Spain (Cesca et al., 2021). In this case, natural gas was injected into a depleted oil reservoir, with the target formation consisting of karstified and fractured limestone. Similarly, the Bavarian Molasse Basin in southern Germany and Switzerland experienced induced seismic events linked to geothermal operations and potentially chemical effects (Seithel et al., 2019). At two of the sixteen hydro-geothermal sites near Munich, seismic events with magnitudes exceeding 2.0 were reported. The largest events occurred during production at the Unterhaching and Poing doublets; earthquakes with local magnitudes of M_L 2.4 and M_L 2.1, respectively, were felt near the injection wells. Additionally, across the German-Austrian border in Sankt Gallen, Switzerland, an M_L 3.5 event was recorded during geothermal well control activities (Diehl et al., 2017). The geothermal targets in these regions mainly consisted of permeable, karstified limestone formations.

Also in the Netherlands & Belgium, induced seismicity has been linked to geothermal production in carbonate reservoirs. In the Californie wells, north of Limburg, two doublets targeted the Dinantian carbonate formation of the Zeeland group. From 2015 to 2018, the KNMI has measured 17 earthquakes with magnitudes between (M_L) -1.2 and (M_L) 1.7 (Baisch and Vörös, 2018; Baisch and Vörös, 2019). Several factors suggested a potential link between geothermal operations and seismic activity. The hypocentres of these events were located near the doublets, but at greater depths, and the timing of the earthquakes often aligned with production reductions or shutdowns. These events may plausibly be attributed to a combination of pressure depletion and thermal effects on a fault that was already in a critically stressed state (Baisch and Vörös, 2018; Baisch and Vörös, 2019). In Balmatt, Belgium, the same carbonate rock formations have been targeted for geothermal energy production. In 2019, a seismic event with a local magnitude (M_L) of 2.1 was induced. This event was associated with the reactivation of a fault located near the injection well (Buijze et al., 2019).

From these events, a pattern was observed in which induced seismicity in carbonate rock reservoirs is closely associated with geothermal energy production, across different carbonate rock types, including mudstone to packstone in Belgium and the Netherlands, and wacke and packstones in Bavaria (Dussel et al., 2018), as well as grainstones in Spain. A common feature is that most of the carbonate reservoirs are fractured, which makes them already sensitive to changes in in-situ stresses. In this case, small changes can be triggered by temperature or chemical effects. We want to investigate whether this could be enhanced by juxtaposing different rock types.

1.6. From field scale to laboratory scale

In order to understand the larger scale, it is important to take a step back and understand what happens on a smaller scale and understand the deformation mechanisms that take place before, during and after fault reactivation. Laboratory experiments are a practical and cost-effective way to systematically investigate the effect of a given set of parameters on individual outputs, which aids in understanding the larger and more variable system

Fault reactivation can be tested in the laboratory with multiple setups. Figure 1.4 visualises the four common options: triaxial experiments with an inclined fault plane, direct shear assemblage, the double direct shear method and rotary shear experiments. Option (a) shows the triaxial shear test with an inclined fault plane. Here, a cylindrical sample with an inclined fault is tested. This allows for the use of confining pressure to provide both shear and normal stress, as well as temperature. Setup (b) shows a direct shear test, a simple test for determining both normal and shear stresses. It is often performed in a direct shear box, which is typically operated without confining pressure and temperature, although it can also be conducted in pressure vessels. Option (c) shows the double shear test, where a central block is sheared between two fixed blocks, allowing symmetric slip along two fault planes. This is commonly performed without confining pressure, but can also be performed at a specific temperature. Option (d) presents the rotary shear setup, in which two surfaces rotate against each other under controlled stress to simulate continuous slip and high strain rates. All setups enable us to study the effect of displacement-driven fault reactivation by directly or indirectly perturbing normal stresses on the fault, or injection-driven fault reactivation by altering pore fluid pressure.

In this thesis, we will only use the triaxial shear setup with an inclined fault plane (Figure 1.4a). The investigation will examine the impact of indirectly altering normal stresses (displacement-driven fault reactivation) and pore pressure (injection-driven fault reactivation) on the fault.

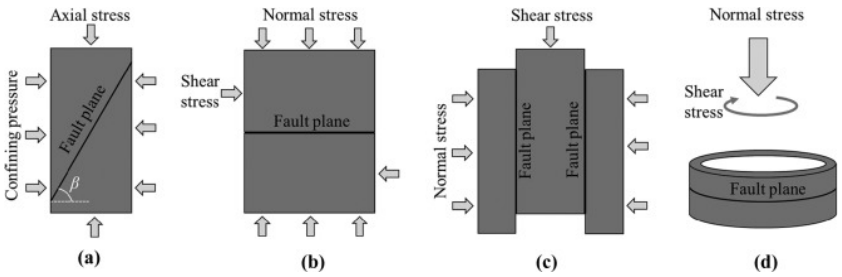

Figure 1.4: Overview of different laboratory setups (Ji, Hofmann, et al., 2022)

Multiple experimental studies have performed triaxial testing on sawcut samples of different rock types. Ji, Zhuang, et al.; Ji, L. Wang, et al.; Ye and Ghassemi have performed a combination of displacement and injection-driven experiments on granite. They tested both monotonic and cycling injection by creating a borehole in the sample itself, as granite has low porosity. Additionally, sandstones are also tested in a similar configuration as in this thesis before (Veltmeijer et al., 2024). Nevertheless, there are no experimental studies on carbonate laboratory fault reactivation that focus on geological heterogeneities in a triaxial setup. Therefore, we will focus on laboratory fault reactivation of carbonate rocks with different geological and hence geomechanical heterogeneities.

1.7. Research Question(s)

How do geological heterogeneities and variations in mechanical properties influence laboratory fault reactivation and shearing behaviour?

- What are the implications of variations in mechanical properties for laboratory fault reactivation and shearing behaviour? How does this relate to the Mohr-Coulomb stress on the fault at reactivation?
- How does fault roughness affect the reactivation of laboratory faults? How does this relate to the mechanical properties of the rock?
- What is the effect of pore pressure on the reactivation of critically stressed laboratory faults? What is the influence on the mechanical properties?
- What are the implications of these findings for induced seismicity in geothermal carbonate reservoirs?

1.8. Workflow

To answer the research question in a structured way. An experimental and analytical workflow has been developed. Given the experimental nature of the study, an experimental plan is implemented to ensure consistency and reproducibility. Figure 1.5 gives the outline of the thesis.

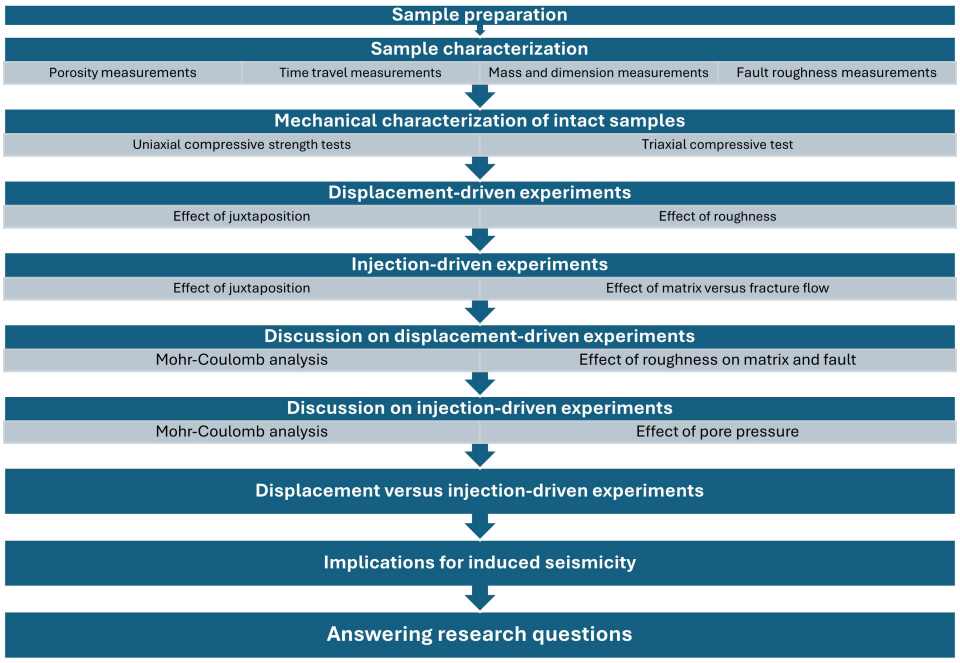

Figure 1.5: Schematic representation of the structure of the thesis

2

Background information

This chapter provides additional background for the thesis by explaining the key concepts and principles that will be referenced throughout the study.

2.1. Definition of stress and strain

This framework adopts the convention of expressing compressive stresses and strains as positive, following the widely accepted method in rock mechanics (Jaeger, N. G. Cook, and Zimmerman, 2007; Fjaer, 2010). The principal stresses, σ_i, are defined such that σ_1 represents the axial stress, while σ_2 and σ_3 act in the radial direction, corresponding to the confining pressure. The stress conditions are given by $\sigma_1 > \sigma_2 = \sigma_3 = P_c$.

The mechanical behaviour of rocks is governed by their intrinsic properties. This includes heterogeneity, porosity and anisotropy (Fjaer, 2010). Additionally, the presence of fluids within the pore space also affects its mechanical response. Therefore, the concept of effective stress is introduced, which is defined as:

$$\sigma' = \sigma_n - \alpha P_p \tag{2.1}$$

where σ' represents the effective stress, σ_n is the normal stress, α is the Biot coefficient, dependent on the rock, not all pore pressure reduces the effective normal stress, and P_p denotes the pore pressure.

2.2. Mechanical properties

When a rock sample is subjected to stress, it undergoes deformation, a process that typically occurs in multiple stages at room temperature. In the initial stage, the sample starts to settle by crack closure. Consequently, the sample experiences elastic deformation, where the stress-strain curve remains linear, and the deformation is fully reversible. However, as stress continues to increase, the behaviour of the sample deviates from the linear part, approaching the yield point. Beyond this point, the deformation becomes plastic, and unstable fractures begin to form. The rock fails once these fractures propagate to a critical extent. An overview of the axial stress-strain diagram is provided in Figure 2.1.

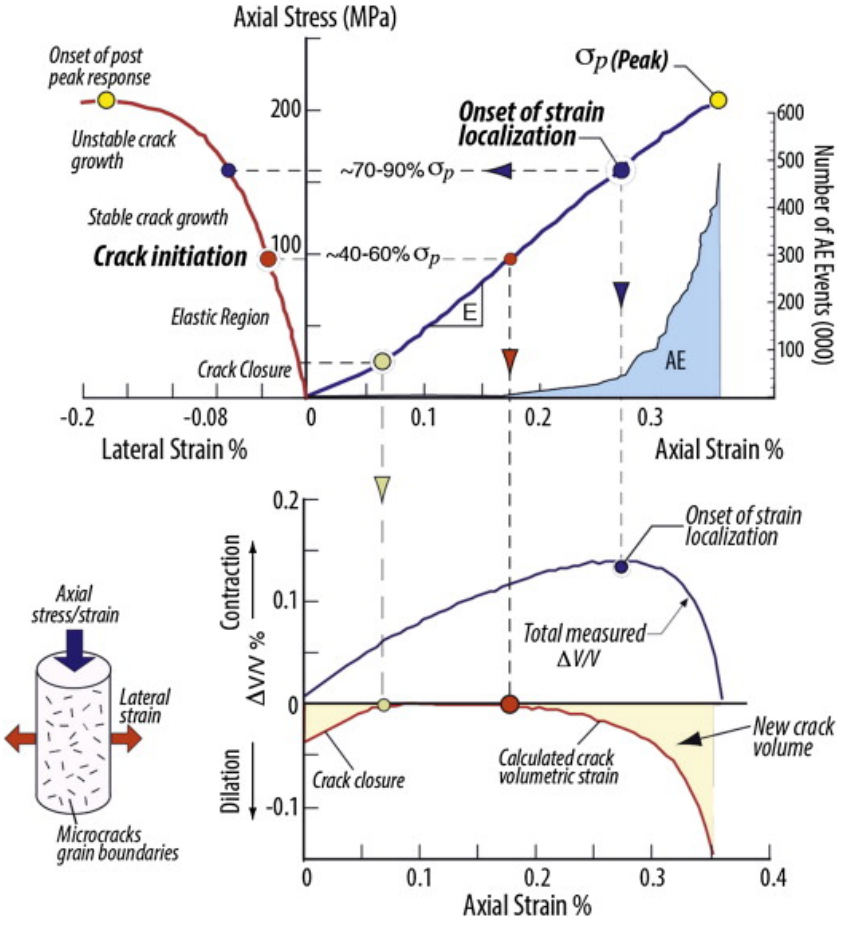

Figure 2.1: Stress-strain curve divided into stages of failure (E. Hoek and Martin, 2014)

In the linear part of the diagram, a linear relationship is observed. This region is referred to as the elastic region. From this region, the Young's Modulus (E) can be determined, as shown in Equation 2.2 and describes the stiffness of a rock. Hence, it quantifies the magnitude of elastic deformation and is expressed in gigapascals (GPa).

$$E = \frac{\Delta\sigma_1}{\Delta\epsilon_1} \tag{2.2}$$

In a similar method, we obtain the Poisson's ratio of a rock sample. Poisson's ratio denotes the lateral expansion relative to the radial expansion. Therefore, it quantifies the directional deformation of the rocks and is unitless. We determine the Poisson's ratio in the linear part of the axial Stress vs axial and radial strain diagram Equation 2.3:

$$\nu = -\frac{\Delta\epsilon_{2,3}}{\Delta\epsilon_1} \tag{2.3}$$

These properties are part of the elastic moduli. They can be determined either through direct experimental measurements, as described above, or indirectly using P-wave and S-wave velocities along with density (ρ in kg/m^3), which are used in empirical correlations with the elastic moduli. When obtained through direct mechanical testing, they are known as static moduli, whereas when derived from wave propagation characteristics, they are referred to as dynamic moduli.

2.2.1. Dynamic elastic moduli

Dynamic elastic moduli are determined based on the velocities of P and S waves and the density of the material. The P-wave represent the longitudinal motion and is also known as the compressional wave. This wave has the fastest arrival time. In contrast, the S-wave, or shear wave, propagates transversely and travels at a slower speed through the rock (Fjaer, 2010). We calculate the velocities (V_p, V_s) with Equation 2.4 where s is the sample length and t the travel time.

$$v = \frac{s}{t} \tag{2.4}$$

We determine the shear modulus (G) and Poisson's ratio (ν) by using the velocities of these waves along with the density of the sample (ρ). The shear modulus characterises the resistance of the material to shear deformation and is expressed in GPa. We utilise the aforementioned parameters to calculate Young's modulus (E) and the bulk modulus (K), which quantify its resistance to uniform compression in GPa, using the following relationships:

$$G = \rho V_s^2 \tag{2.5}$$

$$\nu = \frac{V_p^2 - 2V_s^2}{2(V_p^2 - V_s^2)} \tag{2.6}$$

$$E = 2G(1 + \nu) \tag{2.7}$$

$$K = \frac{E}{3(1 - 2\nu)} \tag{2.8}$$

2.2.2. Static elastic moduli

Based on experimental data, Young's modulus (E) and Poisson's ratio (ν) can be directly determined as described in section 2.2. The remaining elastic moduli can then be computed using these values, as described in Equation 2.9 and Equation 2.8:

$$G = \frac{E}{2(1 + \nu)} \tag{2.9}$$

2.3. Mohr-Coulomb failure criterion

The Mohr-Coulomb failure envelope is a widely used failure criterion in rock mechanics to describe rock failure and/or fault reactivation. This method uses a set of linear equations in the coordinate frame of principal stresses over shear stress (Labuz and Zang, 2014). Originally developed from Mohr; Coulomb, this criterion has been adapted for geomechanical applications (Jaeger, N. G. Cook, and Zimmerman, 2007; Fjaer, 2010) and can be expressed as shown in Equation 2.10.

$$\tau = c + \mu(\sigma_n - P_p) \tag{2.10}$$

where τ is the shear stress on the fracture plane, c represents the cohesion of the fracture, μ is the coefficient of internal friction, σ_n is the normal stress acting on the fracture plane, and P_p is the pore pressure.

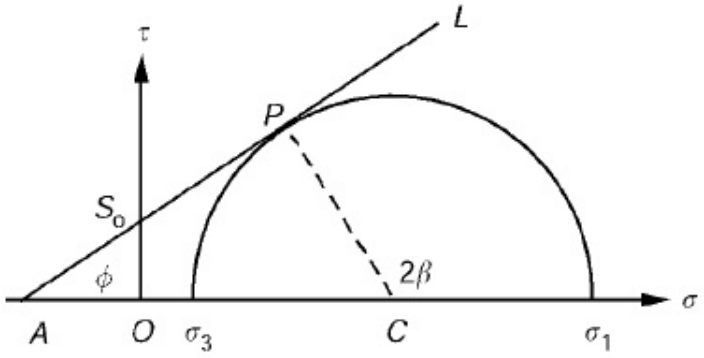

Figure 2.2: Visualization of the Mohr-Coulomb failure envelope (Jaeger, N. G. Cook, and Zimmerman, 2007)

Here, it is important to note that a pre-existing fault is easier to reactivate than to break an intact rock because its cohesion is lower or non-existent, i.e. c approaches zero (Byerlee, 1978; Buijze et al., 2019). With that, the angle of internal friction ϕ is given as $\phi = tan^{-1}\mu$. If the half circle is below this line, it is in a safe stress condition; however, if the half circle touches the line at point P, the rock will fail because of shear stress. At this point P, where the circle is tangent to the Mohr-Coulomb envelope, the critical stress failure angle is represented as 2β. Since $2\beta = 180° - \angle ACP$ and $\angle ACP = 180° - \angle CPA - \angle CAP = 180° - 90° - \phi$. The failure angle can be described as a function of the angle of internal friction as follows, $\beta = 45° + \frac{1}{2}\phi$.

Furthermore, the shear and normal stresses at failure can be determined using Mohr's Circle as represented in Figure 2.2, where the radius R and centre C of the circle are given by:

$$R = \frac{1}{2}(\sigma_1 - \sigma_3) \tag{2.11}$$

$$C = \frac{1}{2}(\sigma_1 + \sigma_3) \tag{2.12}$$

where σ_1 and σ_3 represent the major and minor principal stresses, respectively.

At failure, the coordinates of the shear stress τ and normal stress σ_n can be expressed as functions of the angle 2β, which corresponds to the orientation of the failure plane within Mohr's Circle. To determine the shear stress τ and normal stress σ_n the following equations are used:

$$\tau = R\sin(2\beta) \tag{2.13}$$

$$\sigma_n = C + R\cos(2\beta) \tag{2.14}$$

When pore pressure is also considered, the effective normal stress needs to be used. The equation can be written as:

$$\sigma'_n = \frac{1}{2}(\sigma_1 + \sigma_3 - 2P_p) - \frac{1}{2}(\sigma_1 - \sigma_3)\cos(2\beta) \tag{2.15}$$

Here, τ represents the shear stress acting on the fault plane, while σ_n denotes the corresponding normal stress acting on the fault, and P_p represents the pore pressure in the sample. For this failure

criterion, only σ_1 and σ_3 are considered since this half circle creates the biggest radius as $\sigma_1 > \sigma_2 > \sigma_3$. Additionally, in triaxial experiments $\sigma_2 = \sigma_3$.

To determine the dynamic friction coefficient, the following equation can be used:

$$\mu = \frac{\tau}{\sigma'_n - P_p} \tag{2.16}$$

2.4. Surface roughness classification

Surface roughness can be classified in multiple ways. For this study, we will elaborate on methods that look at the amplitude of the roughness profile and methods that consider the self-similarity of a profile.

A relatively simple method that is commonly used is the Arithmetic average height. Here, roughness is determined based on the average height of the profile (Gadelmawla et al., 2002). Therefore, this method is easy to use, but it does not capture the distribution of the amplitude over the asperities. The formula is given in Equation 2.17.

$$R_a = \frac{1}{l} \int_0^l |y(x)| dx \tag{2.17}$$

Here, R_a denotes the arithmetic average height, while l represents the length of the surface considered and the function $y(x)$ describes the roughness profile as a function of distance.

The second method that is already more sensitive is the Root mean square roughness, which provides a statistical presentation of surface roughness. The RMS quantifies the standard deviation of the distribution of the heights (Gadelmawla et al., 2002). The RMS can be determined as in Equation 2.18.

$$R_{rms} = \sqrt{\frac{1}{l} \int_0^l y(x)^2 dx} \tag{2.18}$$

In this equation, R_{rms} is the RMS roughness, l is the evaluated length and $y(x)$ is the surface profile as a function of distance.

Another method used for characterising surface roughness is the fractal dimension. This mathematical concept was introduced to describe the irregular geometry of coastlines (B. Mandelbrot, 1967), and was later adapted for the analysis of surface roughness (Brown, 1987). The fractal dimension quantifies the relationship between the number of self-similar parts and the scale reduction ratio, using a logarithmic expression (B. Mandelbrot, 1985). Fractal dimensions can be calculated as in Equation 2.19.

$$D = \frac{Log(N)}{Log(\frac{1}{r})} \tag{2.19}$$

In this equation, D represents the fractal dimension, N is the number of self-similar segments used to describe the surface, and r describes the scaling factor. A value of D=2 corresponds to a self-similar surface, hence a smooth surface, while D=3 represents a rough surface with irregular asperities. Subsequently, the fractal dimension captures how ordered or chaotic the roughness is across scales.

Finally, the Hurst exponent is also used to quantify surface roughness. This method was developed to study long-term storage capacities in hydrological systems (Hurst, 1951), but was later adopted to analyse surface roughness. The Hurst exponent, denoted by H, can be computed based on different approaches. In this study, we focus on the rescaled range (R/S) approach. The Hurst exponent also says something about the self-similarity of a roughness profile and the spatial correlation Equation 2.20 (B. B. Mandelbrot and Wallis, 1969). The formula can be written as:

$$\frac{R}{S} \propto \tau^H \quad ; \quad H = \frac{\log\left(\frac{R}{S}\right)}{\log(\tau)} \tag{2.20}$$

Here, R represents the minimum and maximum values of the roughness profile, while S is the standard deviation of the series, and τ is the measured period in the series. Its value ranges between 0 and 1, where higher values represent smoother, more correlated surface features, while lower values indicate rougher, more irregular patterns.

2.5. Darcy's Law

To describe flow through a porous rock sample, we use Darcy's law. The formula used to describe single-phase flow can be written as:

$$q = -\frac{k}{\mu} A \frac{dp}{dx} \tag{2.21}$$

Where, q is the volumetric flow rate (m^3/s), k is the permeability of the medium (m^2), μ is the dynamic viscosity of the fluid (Pas), A is the cross-sectional area to flow (m^2), $\frac{dp}{dx}$ is the pressure gradient along the sample (Pa/m).

If we want to determine the permeability in a rock sample, we need to rewrite the equation so that:

$$k = -\frac{q\mu}{A} \frac{dx}{dp} \tag{2.22}$$

3

Methodology

This chapter describes the methodology we used for data acquisition and analysis. We tested two different carbonate rock samples through various experiments. First, we conducted unconfined compression tests (UCS) on intact samples of Indiana limestone and Dinantian carbonate. We saturated the Indiana limestone samples with DI water and the Dinantian carbonate with both DI water and Brine obtained from Vito. These UCS tests provided the mechanical properties of the rock samples.

Following this, we performed three triaxial compressive stress tests on dry Indiana limestone and DI water-saturated Indiana limestone, as well as DI water-saturated Dinantian carbonate. Consequently, we performed displacement-driven experiments using a triaxial compressive stress test setup. The carbonate rock samples were saw-cut at an angle of 35°using three different methods to test fault surface roughness. These tests were performed under a confining pressure of 35 MPa. Additionally, we conducted some repeat experiments to ensure reproducibility. We performed these experiments for three different configurations: (1) Dinantian, (2) Indiana limestone, and (3) a mixed configuration combining both rock types. We also received data from one saw-cut experiment on Indiana limestone in this series of experiments.

Afterwards, we performed injection-driven experiments for all three configurations with a saw-cut surface roughness. Here, we critically stress the fault and introduce the effect of pore pressure to reactivate the fault. In this procedure, we also performed the permeability test.

3.1. Sample material

The Dinantian carbonate samples we used were mostly composed of calcium carbonate and had a low porosity of 2.19% $\pm$ 0.98 %. In the literature, a wide variety of interpretations exist based on the Dunham classification. Depending on the location and depth, it is interpreted as mudstone and even grainstone (Reijmer et al., 2017; Mozafari et al., 2019). The samples used in this study are visually classified as either mudstone or wackestone. The Dinantian carbonates used for experiments with code MLD are from an outcrop in L'Hoist, Belgium. The Indiana limestone is mostly composed of calcium carbonate (97%) and has a porosity of 16.53% $\pm$ 0.62% (Hart and H. F. Wang, 1995). The Indiana limestone can be characterised as a grainstone using the Dunham classification (Walton et al., 2017). The samples used are from a quarry in Indiana, United States. In Table 3.1 we provide some of the dry rock properties.

Table 3.1: Dry rock properties

Rock Type	Measured density (g/cm^3)	Porosity (%)	P-wave (km/s)	S-wave (km/s)
Dinantian carbonate	2.84 $\pm$ 0.01	2.19% $\pm$ 0.98 %	4.85 $\pm$ 0.52	3.02 $\pm$ 0.27
Indiana limestone	2.69 $\pm$ 0.01	16.53% $\pm$ 0.62%	3.99 $\pm$ 0.13	2.35 $\pm$ 0.06

3.2. Sample Preparation

To prepare the samples for the experiments, we used the following procedure:

1. **Core Drilling**: All samples were drilled with a diameter of 30 mm from a larger rock block obtained from the previously mentioned locations.
2. **Sawing to Required Dimensions**:
   - We cut the UCS samples with a water-based cutter to a length of 59.7 $\pm$ 0.5 mm.
   - We cut the triaxial test samples with a water-based cutter to a length of 75.23 $\pm$ 0.76 mm
3. **Drying**: All samples were dried overnight in an oven at 60°C.
4. **Porosity Measurements**: The connected porosity of the samples was determined using a helium pycnometer. In this method, the matrix volume is measured and used, together with the calculated bulk volume, to determine the porosity.
5. **Travel Time Measurements**: we measure the P-wave and S-wave travel times using an active acoustic setup, where a source generated a 700 mV signal at 1 MHz Figure 3.1. This device measures the travel times, from which the velocities can be determined with the sample lengths.

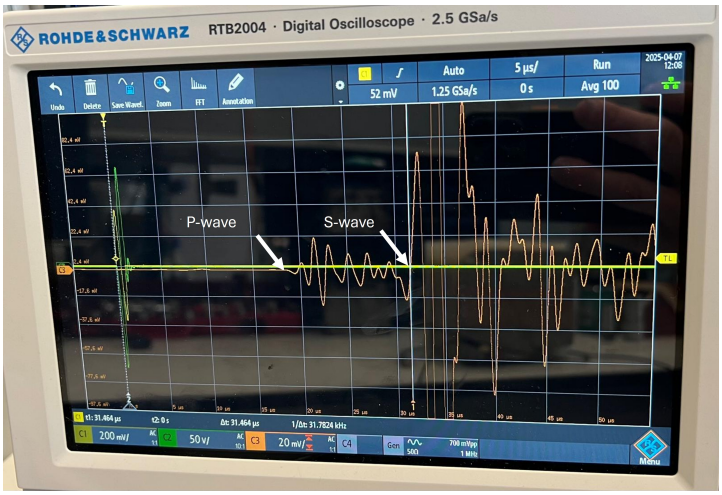

Figure 3.1: Active acoustics to measure P and S-wave travel times

6. **Saturation and Additional Measurements for UCS Samples and Intact Triaxial Samples**: After obtaining the dry-state P- and S-wave velocities, we saturated the samples with deionised water and brine and repeated the velocity measurements. We additionally measure the mass of the samples before and after saturation with an accuracy of 0.001 g.
7. **Hole Drilling for Injection-driven Dinantian Carbonate samples**: For the injection-driven experiments, one additional step was needed for the Dinantian carbonate samples before cutting. Since matrix permeability is low, we needed to drill a hole in the intact Dinantian carbonate samples to stimulate flow. This was done with a diameter of 3.3 mm.
8. **Cutting for Displacement-driven and Injection-driven Triaxial Tests**: For the displacement-driven tests, we created three different fault roughness patterns. In the first method, we saw-cut the sample with a water-based cutter at an angle of 35 ° and utilised the surface obtained under the name saw-cut roughness. The handmade roughness is created in the same way, but then we modify the fault profile by adding grooves every 3 mm. We do this with a file and a pin drill. The last roughness profile was created using a waterjet. To ensure that the profiles fit together, the cylindrical-shaped sample is placed in gypsum to regain a rectangular shape, allowing for better cutting with the waterjet. Here we cut the intact rock in a specific profile. For injection-driven experiments, we only used the saw-cut roughness.
9. **Drying of Saw-Cut Samples**: All cut samples were dried overnight in an oven at 60°C.

10. **Surface Roughness Measurements**: We measured all roughness profiles once using a Keyence Instant 3D Profilometer VR-6000 at high magnification (40x) in high-resolution mode. We do this to characterise the surface roughness using the Root Mean Square (RMS) method.
11. **Tiny Permeabilty Measurements**: Before the injection experiments, we measured the tiny permeability of the Indiana limestone samples with a TinyPerm 2 portable air permeameter. We did this to obtain an indication of the sample's permeability.
12. **Sample Saturation** Before we performed the triaxial experiments, we saturated the samples in 100 mL DI water under compression. We do this for one hour for the Indiana limestone and overnight for the Dinantian carbonate. We additionally measure the mass of the samples before and after saturation with an accuracy of 0.001 g.

3.3. Experimental setup

3.3.1. Uniaxial compression experiments

We performed the experiments using a servo-controlled uniaxial loading machine at TU Delft, with a max loading capacity of 500 kN and accuracy of ± 0.05 kN. In this setup, Linear Variable Differential Transformers (LVDT) measure the axial displacement (accuracy of ± 0.1 μm), and a chain with an embedded sensor captures the radial strain. For the UCS tests, the experimental configuration is shown in Figure 3.2. During the experiment, the displacement of the rock and the machine is measured. Therefore, a correction for axial strain is applied as explained in subsection A.1.1.

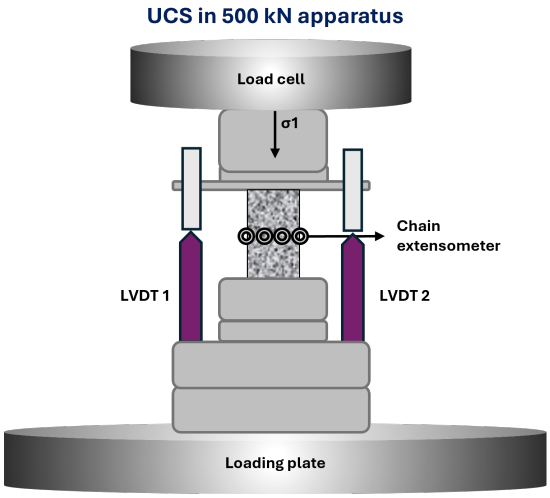

Figure 3.2: Experimental setup for UCS

3.3.2. Triaxal compression experiments

We also utilised the 500 kN machine for the triaxial compression tests (Figure 3.3). In this setup, a Hoek cell was used (Evert Hoek and Franklin, 1968) to apply a confining stress. The Hoek cell is a cylindrical steel chamber containing an internal sleeve that isolates the confining fluid from the rock sample. The confining pressure was applied through an inlet on the side, controlled by an ISCO 100DM pump. The sample was loaded from the top, where the load cell is present, and we controlled the displacement of the bottom plate. We placed the sample between two loading pistons, which can also be used for fluid injection and active and passive acoustic measurements. The pistons had a hemispherical outer shape, fitting into a correspondingly shaped plate to ensure proper vertical alignment. Consequently, two other ISCO 100DM pumps were used to apply a pore pressure in the system with DI water. Additionally, a delta pressure sensor was attached to the setup to measure the pressure difference between the tubes closer to the sample. The fluid was injected from the bottom of the sample with an injection pump, while the top was attached to the reservoir pump. In this setup, we positioned the LVDTs at the loading plate and will need correction experiments as described in subsection A.1.2.

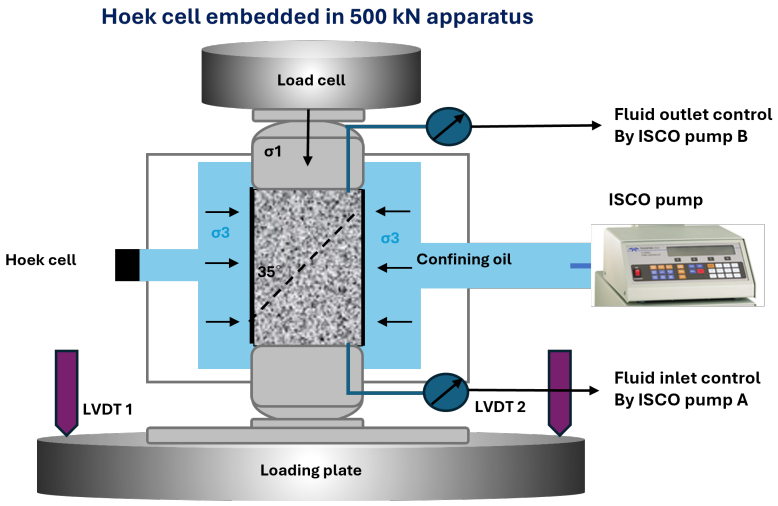

Figure 3.3: Experimental setup for Triaxial compressive test with Hoek cell

3.4. Experimental plan

3.4.1. Uniaxial compressive experiments

In Table 3.2 we present the experimental plan for the UCS tests. Here, a sample ID of MLD represents the Dinantian carbonate and ID the Indiana limestone. In the UCS experiments, we tested mechanical properties for two rocks. We also tested the effect of fluid saturation in the Dinantian carbonate. We performed the experiments under atmospheric pressure and at room temperature.

Table 3.2: Experimental plan for UCS tests

Sample ID	Porosity (%)	Saturation (Overnight)
MLD1-B9	1.01	DI water
MLD1-B10	0.80	DI water
MLD1-B12	0.55	DI water
MLD2-C1	2.74	Brine
MLD2-C2	2.64	Brine
MLD2-C3	2.92	Brine
MLD2-C4	3.78	Brine
MLD2-C7	3.48	Brine
MLD2-C8	3.26	Brine
MLD2-C9	2.69	Brine
MLD2-C10	2.00	Brine
ID3	17.18	DI water
ID4	17.30	DI water
ID5	17.38	DI water
ID6	17.30	DI water

3.4.2. Triaxial compressive experiments on intact rocks

In Table 3.3 we represent the experimental plan for the triaxial experiment on intact samples at a confining pressure of 35 MPa. MLD samples represent the Dinantian carbonate, and I represents the Indiana limestone samples. In these experiments, we tested the effect of surface roughness on the reactivation of laboratory faults, as well as the impact of heterogeneity. We performed the experiments at room temperature.

Table 3.3: Experimental plan for Triaxial compressive tests on intact rocks

Sample ID	Porosity (%)	Confining pressure (MPa)	Saturation
I-2	15.99	35	DI water 1 hour
I-8	17.00	35	Dry
MLD7-44	1.63	35	DI water overnight

3.4.3. Triaxial compressive displacement-driven experiments

In Table 3.4 we visualise the experimental plan for the displacement-driven experiments on faulted rock samples. MLD samples represent the Dinantian carbonate, and I represents the Indiana limestone samples. In this experiment, we reactivate the sample by increasing the axial stress after hydrostatic conditions. We performed the experiments at room temperature.

Table 3.4: Experimental plan for displacement-driven experiments

Sample ID	Confining Pressure (MPa)	Type of Roughness	Saturation (DI Water)
I-6-21	35	Saw-cut	1 hour
I-4	35	Saw-cut	1 hour
I-7-9	35	Handmade 1	1 hour
I-10_1	35	Handmade 2	1 hour
I-13	35	Waterjet	1 hour
MLD7-28-45	35	Saw-cut	Overnight
MLD7-34	35	Handmade	Overnight
MLD7-35	35	Waterjet	Overnight
MLD7-40	35	Waterjet	Overnight
MLD7-36-I-11	35	Saw-cut	Overnight – 1 hour
I-11-MLD7-36	35	Saw-cut	1 hour – Overnight
MLD7-30-I-14	35	Waterjet	Overnight – 1 hour
I-14-MLD7-30	35	Waterjet	1 hour – Overnight

3.4.4. Triaxial compressive injection experiments

We visualise the experimental plan for the injection-driven experiments on faulted rock samples in Table 3.5. MLD samples represent the Dinantian carbonate, and I represents the Indiana limestone samples. In these experiments, we test the effect of pore pressure on the reactivation of critically stressed heterogeneous laboratory faults. We performed the experiments at room temperature.

Table 3.5: Experimental plan for injection-driven experiments

Sample ID	Confining Pressure (MPa)	Pore Pressure Rate (MPa/min)	Type of Roughness	Saturation (DI Water)
I-19-I-18	35	0.5	Saw-cut	1 hour
MLD7-23	35	0.5	Saw-cut	Overnight + 24 hours
MLD7-50-I-15	35	0.5	Saw-cut	Overnight + 48 hours – 1 hour
I-15-MLD7-50	35	0.5	Saw-cut	1 hour – Overnight + 48 hours

3.5. Experimental procedure

3.5.1. Uniaxial compressive experiments

When the sample preparation was finished, we attached the chain extensometer to the sample and placed it inside the 500 kN apparatus. In displacement control, the loading plate is moved upward to apply a small load to the sample. Now that we have aligned the LVDTs with the machine, we can start the recording. When we started the recording, we put the machine in strain control and started loading the sample with a rate of 0.0005 s^{-1}. Once the sample failed, the recording was closed, and the experiment was finished.

3.5.2. Triaxial compressive experiments on intact and fractured samples

After we finish the sample preparation for the triaxial experiments, we can place the samples inside the Hoekcell. When the sample was inside, we mounted the pistons to the Hoekcell and applied a confining stress of 0.1 MPa to secure the Hoekcell within the 500 kN apparatus. To build up to hydrostatic conditions, a scheme was used to incrementally increase the confining stress and axial load in 0.1 MPa increments. Once hydrostatic conditions were reached (35 MPa), we could set the LVDTs and start the recording, and the machine was put into strain control to start loading with a rate of 0.0005 s^{-1}. Once the sample had failed or the LVDTs had finished 2 mm of axial displacement, the experiment was stopped. After the experiment, we unloaded the system in a similar method to how the load was built up.

3.5.3. Triaxial compressive injection experiments and permeability test

In the injection-driven experiments, the same starting procedure is used as in the other triaxial compressive tests. However, we now needed to attach the pipes to induce pore pressure once the Hoekcell was placed in the machine. To make sure that no air is in the system, the pipes and sample are flushed with DI water. Once everything is in place, we begin the experiment. First, we build up to 10 MPa of confining pressure and axial stress to initiate a pore pressure of 2 MPa at a rate of 0.2 MPa/min. Once the pore pressure has built up, we stabilise the system and start building up to hydrostatic conditions. Then we put the system into strain control and build up at a rate of 0.0005 s^{-1} to the fault is critically stressed, which we assume to be 3 MPa before the yield point obtained from the displacement-driven experiments. Then we hold the system in strain control and start building up the pore pressure with a rate of 0.5 MPa/min until the fault reactivates. This pore pressure rate was applied to ensure uniform pressure build-up throughout the sample with matrix flow. Reactivation occurs when the axial stress starts to drop. This happens because less axial stress is needed to maintain the strain constant due to the movement of the fault. Once this happened, we finished the experiment.

Following almost the same starting procedure, we performed the permeability test. However, now we have only reached a confining stress and axial stress of 10 MPa. Then, we applied a constant flow rate of 1, 2, and 3 mL/min to determine the permeability once the system had reached a steady state.

3.6. Data processing

3.6.1. Mechanical characterisation of UCS and triaxial compressive tests

We developed the following method to determine the elastic part of the stress-strain plots. We plotted the stress time derivative (y) versus time (x). The derivative of the stress time should be constant for the elastic-linear part. We selected point A on the graph as the start of the linear part and point B, noting the yield point and thus the point at which plastic deformation begins. For our displacement-driven experiment, point B denotes the reaction point. Figure 3.4 shows an example of our methodology. We observed that the derivative deviates at points A and B, both before and after. Additionally, we noted point C in the UCS tests as the maximum axial stress that the rock can support. Based on the values for the Time of points A and B, we selected the Axial stress, axial strain and radial strain values (only UCS) for the calculation of the static moduli on the methods described in subsection 2.2.2. In our triaxial compressive tests, we used the convention of deviatoric stress. This means that stress and strain were normalised at hydrostatic conditions (P_c = 35 MPa).

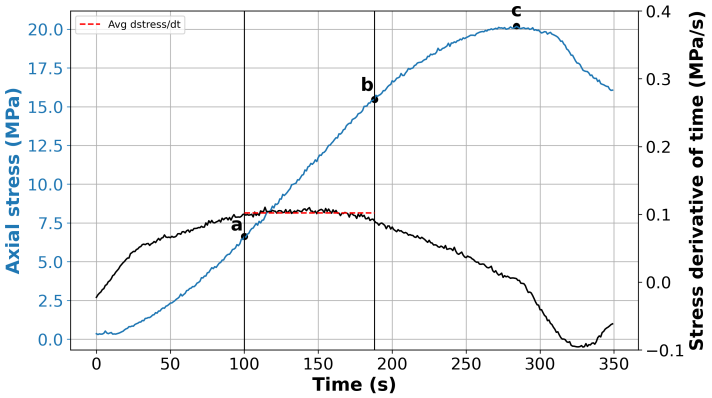

Figure 3.4: Example of stress over time plot with the stress derivative

3.6.2. Injection-driven experiments

In the injection-driven experiment, fault reactivation was observed by a drop in axial stress (Point B). Since the machine is put on hold in strain control during the injection phase of the experiments, the displacement of the LVDTs is constant. If the fault reactivates under displacement-driven conditions, this is typically expressed in terms of displacement along the fault, resulting in increased LVDT readings. However, in the injection experiments, this is kept constant, and therefore, a drop in axial stress is observed to compensate for the displacement. In these experiments, point A is used to determine the effective normal stress and shear stress at the starting point of the injection experiments. Figure 3.5 shows an example of the process.

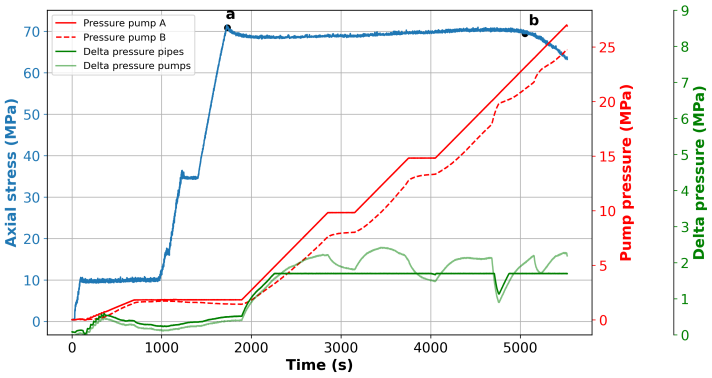

Figure 3.5: Example of stress over time plot for the injection experiments with point A & B. On the right axis, we also visualise the pressure of pump A & B with the difference in pressure between pump A & B and the measurements of the dP.

3.6.3. Fault roughness characterisation

For the characterisation of the roughness, we used the RMS method as described in section 2.4. From the STL data extracted from the profilometer, we create a 3D coordinate system in the x, y, and z directions. Then we normalise the z values so that the lowest point is zero. From the x and y coordinates, we create a 2D grid, where we use the z coordinates to generate a height map. Based on this height map, we created the RMS roughness of the surface. Figure 3.6 shows the chaptered roughenss profiles.

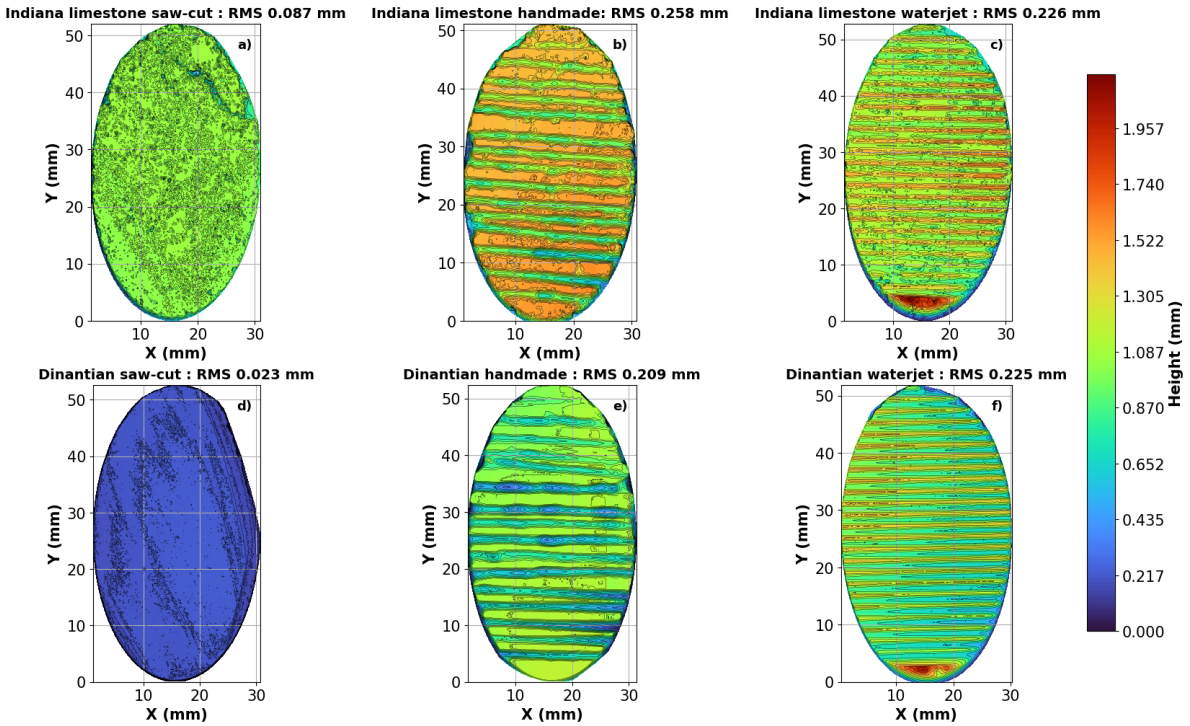

Figure 3.6: Surface profiles of Indiana limestone and Dinantian carbonate: (a,d) corresponds to the Saw-cut configuration, (b,e) illustrates the Handmade profile, and (c,f) represents the Waterjet roughness profile.

4

Results

4.1. Mechanical characterisation of intact samples

4.1.1. Dynamic elastic moduli

We measured the density, matrix density, and acoustic travel times on 22 Indiana limestone samples and 47 Dinantian samples under air-dry conditions, at room temperature, and atmospheric pressure. Then, we vacuum-saturated 3 Dinantian samples and 4 Indiana limestone samples in deionised (DI water) and 8 Dinantian samples in geothermal brine obtained from the Mol geothermal site (Bos and Laenen, 2017) for 18 hours and 1 hour, respectively. The saturation time for the low-porosity carbonate Dinantian samples ensured sufficient time for rock-fluid interaction within a feasible timescale for conducting laboratory experiments. Afterwards, we captured the time travel of the acoustic velocities of the saturated samples.subsection 2.2.1 describes how we deterine these properties. Figure 4.1 shows the effect of sample porosity (lithology) and fluids used on the dynamic elastic properties of the rocks.

An increase in the porosity from the Dinantian carbonate to the Indina limestone results in a reduction in their dynamic Young's modulus, shear modulus, and bulk modulus. Conversely, higher porosity was associated with an increase in Poisson's ratio. Additionally, we observed that fluid saturation resulted in an increase in the dynamic elastic moduli within the Dinantian samples, whereas fluid saturation resulted in a decrease in the dynamic elastic moduli for the Indiana limestone. Furthermore, within the Dinantian samples, brine-saturated samples exhibited higher Young's modulus, Poisson's ratio, and bulk modulus compared to DI water-saturated samples. The shear modulus, however, remained unaffected by the type of saturating fluid.

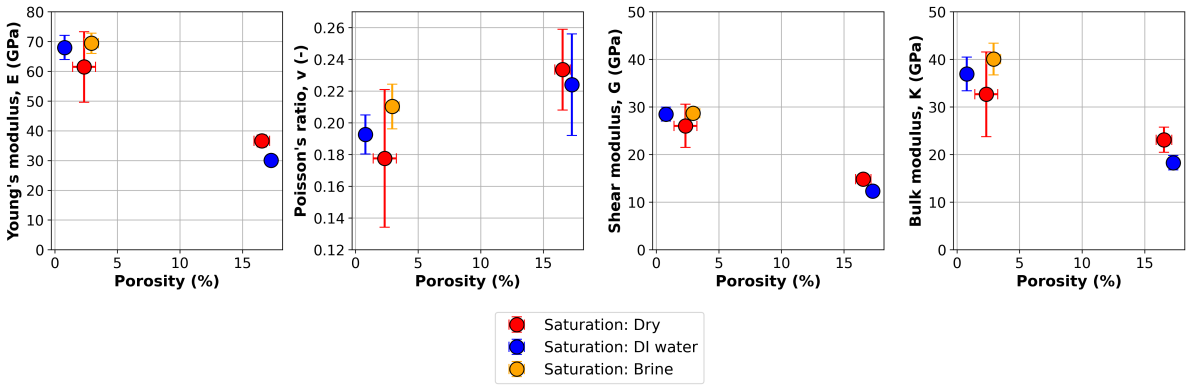

Figure 4.1: Average and 1 standard deviation of dynamic elastic moduli of Indiana limestone and Dinantian carbonate. This includes dry samples and saturated samples in DI water for both Indiana limestone and Dinantian carbonate, as well as Dinantian carbonate saturated in brine.

4.1.2. Uniaxial compression experiments

We conducted 11 UCS experiments using Dinantian carbonate rocks. Of these, 3 were saturated in DI water and 8 in Brine. All 4 tested Indiana limestones are saturated in DI water. Figure 4.2 presents the stress-strain plots (axial and radial) and postmortem pictures after the UCS test for the DI water saturated samples.

We observed that a minor increase (<1%) in the porosity of the Dinatian carbonate samples induced an increase in the slope of the axial stress axial strain curves (stiffness) and UCS (Figure 4.2a). Additionally, samples with a lower UCS exhibited more stress drops after the yield point compared to the sample with the highest UCS. From the beginning of the experiment, we saw a different response in the mechanical behaviour of all samples. Also, we examined the samples post-experimentally and spotted the development of shear fractures characterised by axial splitting (Figure 4.2c).

A minor increase in the porosity of Indiana limestone resulted in a decrease in stiffness and UCS (Figure 4.2b). Consequently, we observed that the mechanical behaviour is homogeneous at the beginning of the experiment. Postmortem Indiana limestone samples did not exhibit major fractures indicative of shear failure/axial splitting (Figure 4.2d)

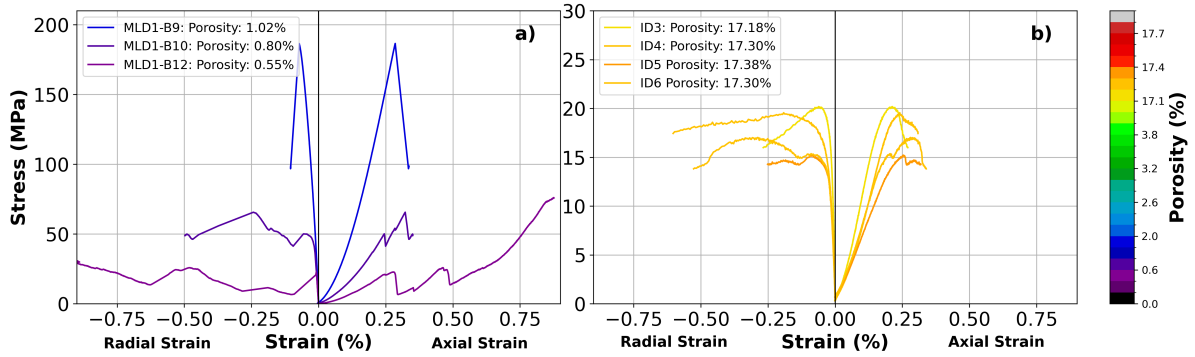

(a) Visualisation of UCS stress-strain data of a) Dinantian carbonate and b) Indiana limestone. The negative values represent the radial strain, while the positive values denote the axial strain of the samples. Additionally, the porosity of the samples is given by the colour bar. (The stress axis is not in the same range.)

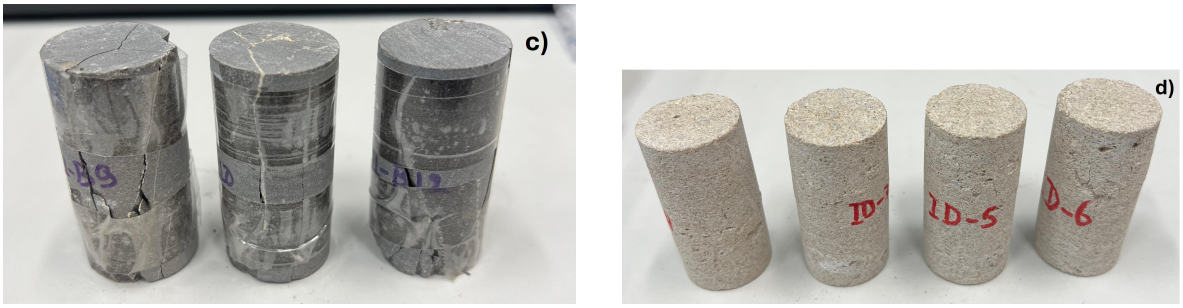

Figure 4.2: Overview of UCS test results. (a, b) Stress-strain curves for Dinantian and Indiana limestone samples. (c, d) Corresponding post-mortem photos of the tested Dinantian carbonate and Indiana limestone samples, respectively.

Figure 4.3 depicts the stress-strain data of the three samples saturated in DI water (a) and the eight samples saturated in Brine (b). The samples were saturated in brine, varied in stiffness and UCS, with no apparent correlation to porosity. The samples saturated with DI water exhibited the same wide variation in stiffness and UCS, however, with a slight to porosity. In both types of fluid saturation, we observed a variation of stress drops ranging from one big stress drop to multiple smaller ones. Postmortem samples exhibited similar behaviour with axial splitting as we observed before.

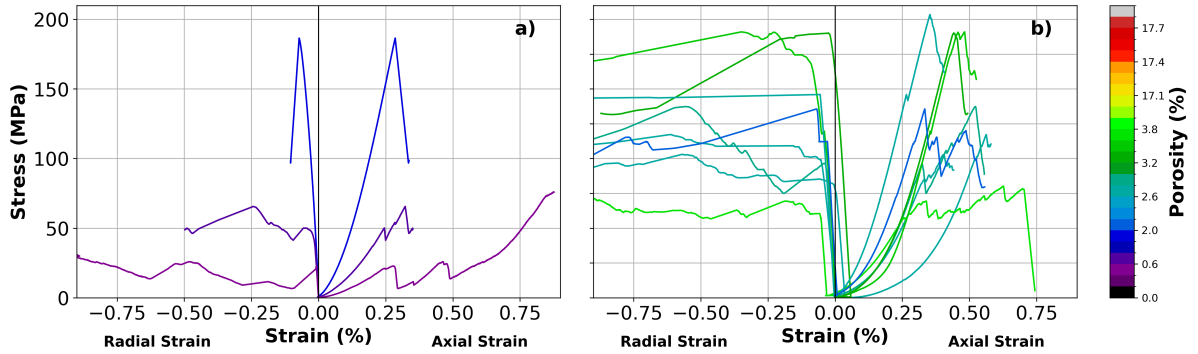

Figure 4.3: Visualisation from the UCS test stress and strain data of Dinantian carbonate saturated in a) DI water and b) Brine. The negative values represent the radial strain, while the positive values denote the axial strain of the samples. Additionally, the porosity of the samples is also integrated.

4.1.3. Uniaxial compressive strength

Figure 4.4 presents the correlation of ultimate compressive strength with porosity. Within the DI water-saturated Dinantian samples, we observed a wide range of UCS in a small porosity range. A similar range is observed for the samples saturated in brine, but for a wide range of porosities. Within the Indiana limestone, there was only a small variation in both UCS and porosity. However, with a larger increase in porosity, the UCS decreases from Dinantian to Indiana limestone.

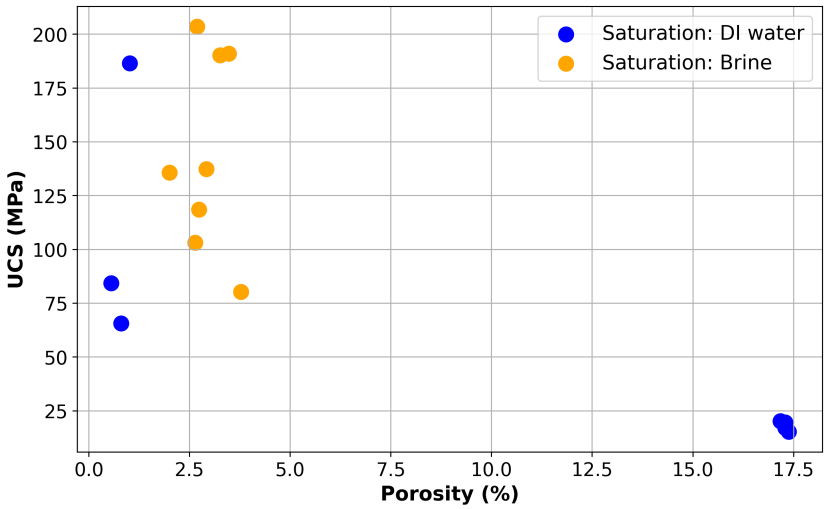

Figure 4.4: Ultimate compression strength versus the porosity. Includes samples saturated in DI water for both Indiana limestone (16.5% porosity) and Dinantian carbonate samples (2.2% porosity), and Dinantian carbonate saturated in brine.

4.1.4. Static elastic moduli

Figure 4.5 visualises the static elastic moduli of the Dinantian carbonate and Indiana limestone samples saturated in DI water and the Dinantian carbonate samples saturated in Brine. We observed that Young's modulus, Shear modulus, and Bulk modulus correlated negatively with sample porosity, while Poisson's ratio correlated positively with sample porosity for the DI water-saturated samples. Dinantian samples also displayed a wider standard deviation than the Indiana limestone samples. Furthermore, Dinantian samples saturated in Brine exhibit higher Young's modulus, Poisson's ratio, shear modulus and bulk modulus compared to the samples saturated in DI water. However, the brine-saturated samples fall within the same standard deviation range as the DI-water saturated.

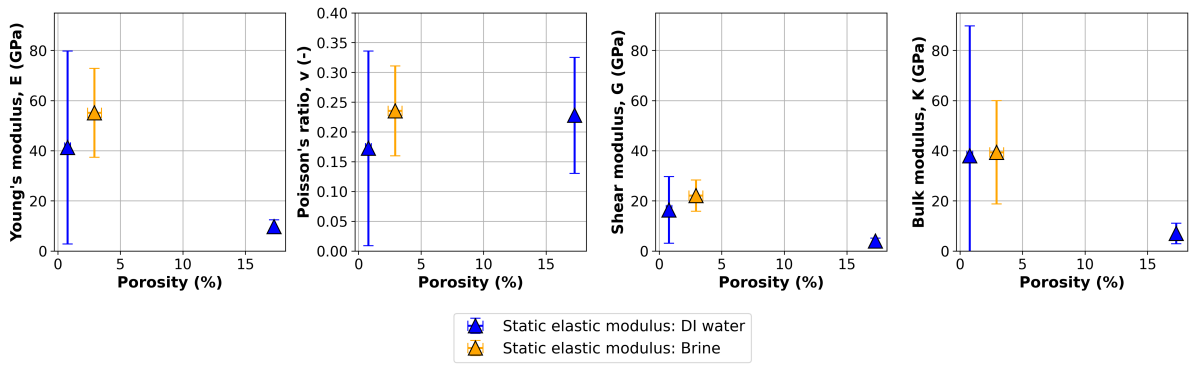

Figure 4.5: Static elastic moduli of Indiana limestone (16.5% porosity) and Dinantian carbonate samples (2.2% porosity), saturated with DI water for both Indiana limestone and Dinantian carbonate, and Dinantian carbonate saturated in brine.

4.1.5. Triaxial compressive experiments

We conducted triaxial experiments with intact Dinantian carbonate and Indiana limestone, at a confining pressure of 35 MPa, in drained conditions, and at room temperature.

We observed that peak strength, yield point and stiffness of the samples correlated negatively with porosity Figure 4.6. The Dinantian sample, which has the lowest porosity, exhibited the highest peak stress, yield point and Young's modulus. It experienced a stress drop beyond the peak strength. Additionally, we detected oblique fractures in the Dinantian samples post-experimentally.

Within the Indiana limestone samples, we observed that peak strength, yield point and stiffness correlated negatively with porosity. However, with the increase in porosity, the conditions also change from wet to dry. (Figure 4.7). From the visual observation, we could see that the Indiana limestone samples were still intact. However, the diameter in the middle of the sample has become thicker than the top and bottom ends.

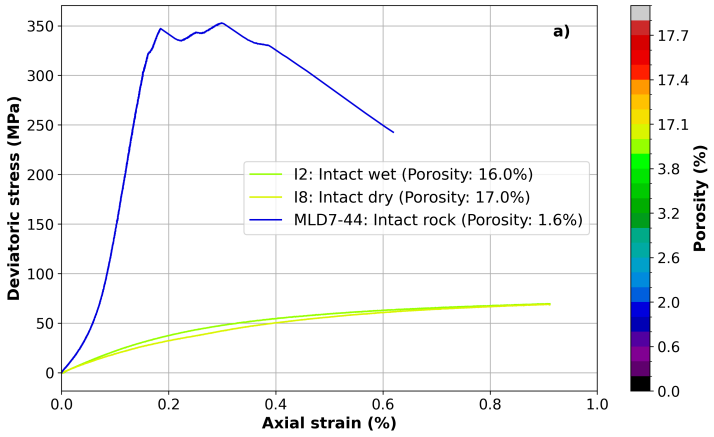

(a) Visualisation of triaxial stress-strain data of Dinantian carbonate and Indiana limestone. Additionally, the porosity of the samples is given by the colour bar.

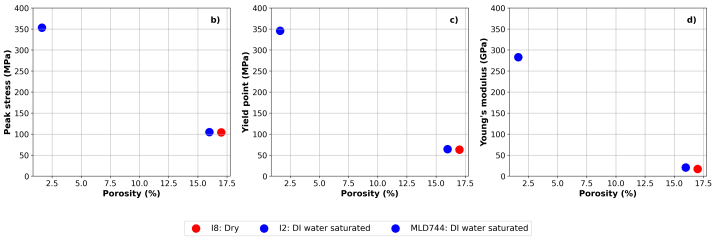

(b) Visualisation of triaxial mechanical data obtained from the mechanical behaviour of the Dinantian carbonate (1.6% porosity) and Indiana limestone (16.5% porosity) at 35 MPa confining pressure. Subplot b) describes the peak stress, c) the Yield point and d) the Young's modulus as a function of porosity.

Figure 4.6: Mechanical behaviour of Dinantian carbonate and Indiana limestone under triaxial conditions at 35 MPa confining pressure.

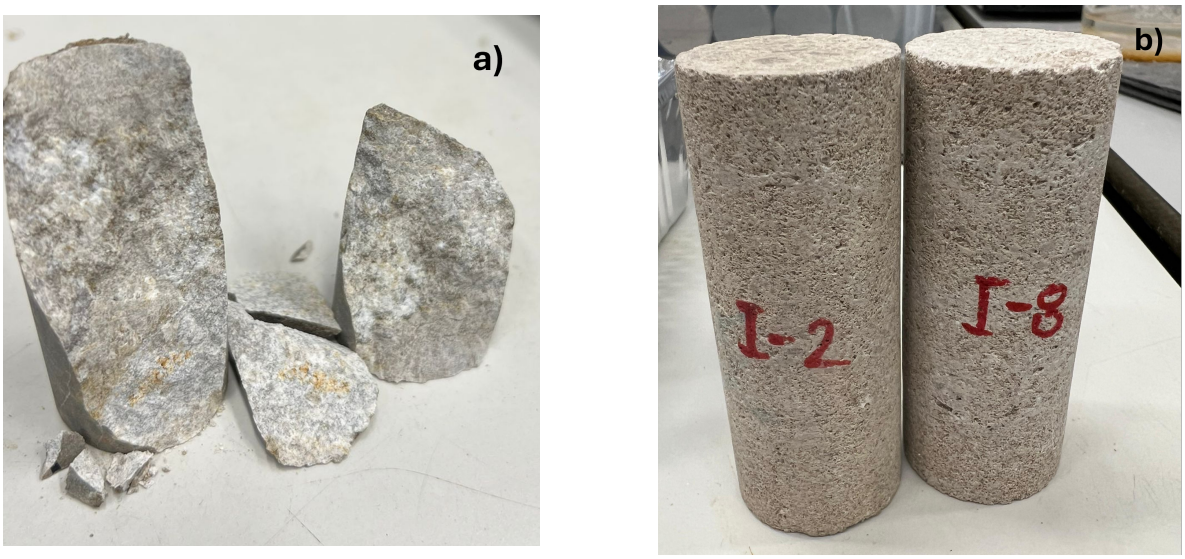

Figure 4.7: Post mortem pictures of triaxial tested a) Dinantian carbonate sample and b) Indiana limestone samples.

4.2. Displacement-driven fault reactivation: effect of surface roughness

Here, we discuss the results obtained from the displacement-driven test on laboratory faults with different roughness profiles. In Figure 4.9 we visualise all the stress-strain plots and mechanical parameters from the different configurations and roughness profiles. Figure 4.10 shows the post-mortem pictures of the samples after the experiment.

4.2.1. Dinantian carbonate

We observed that the stiffness of the system (sample matrix and fault) decreases with an increase in RMS (Figure 4.9a). With this increase in roughness, the sample drifts away from the stiffness of the intact rock. This corresponds with the behaviour in Figure 4.9d. From Figure 4.9g,j, we observed that with increasing roughness, the reactivation stress and axial strain at reactivation increased for the waterjet samples compared to the saw-cut, but for the handmade roughness, the reactivation stress decreased and axial strain at reactivation increased slightly.

For the roughness profiles, we observed clear pre- and post-reactivation behaviour (Figure 4.9a). In Figure 4.8, we elaborate on this behaviour. In green we indicate the buildup of stress, in yellow a constant stress and in red a stress drop. In Figure 4.8a we can see that the saw-cut sample has mainly three phases, with, in the end, a variation with small stress drops and constant stress. We also see that the waterjet sample has 4 different stages with quite constant behaviour (Figure 4.8b). However, in Figure 4.8c we see that the handmade sample experiences multiple more different stages, with twice as another buildup of stress.

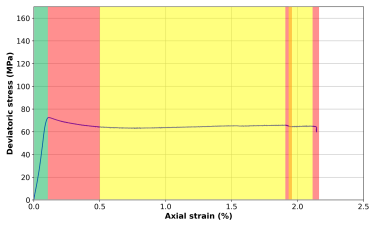

(a) Dinantian saw-cut configuration.

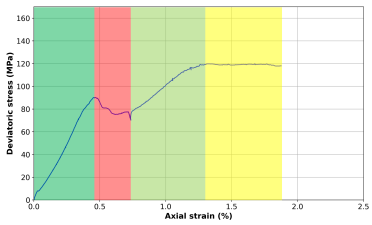

(b) Dinantian waterjet configuration.

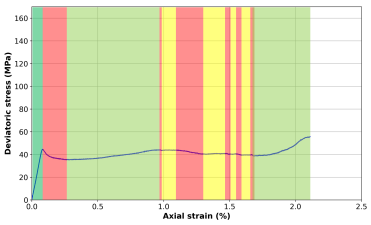

(c) Dinantian handmade configuration.

Figure 4.8: The stress–strain curves are divided into different stress stages: green indicates the initial increase in stress; red denotes a stress drop; yellow represents a period of constant stress; and light green is another buildup in stress

In Figure 4.10a, we see the Dinantian carbonate samples post mortem. Here we can see the lineations slip parallel direction after the experiment for the saw-cut. Additionally, the fault surface has a light whiter surface. In waterjet roughness, we see that all asperities are broken, and we also obtained some recoverable gouge of 0.192 grams. The fault surface is also very white after the experiment. For the handmade, we see that the top asperities are broken with loose material on them, while the grooves are still clear. The colour of this loose rock on the grooves is brownish.

4.2.2. Indiana limestone

Applying the same analysis to the Indiana limestone. We do not directly see a trend with roughness in Figure 4.9b. From Figure 4.9e, we see that the Young's modulus increases slightly with increasing roughness from the saw-cut to the waterjet. However, the handmade profile increases slightly compared to the saw-cut. In Figure 4.9h & Figure 4.9k, we observe that with increasing roughness, the reactivation stress and the strain at the reactivation point decrease.

When focusing on the behaviour after reactivation, we observe in Figure 4.9b that the saw-cut and waterjet samples exhibit behaviour similar to the intact rock, whereas the handmade roughness deviates after reactivation. The general trend for the intact, saw-cut, and waterjet configurations is a gradual stress increase, characterised by strain hardening. Here,

If we look at the Indiana limestone sample before and after the experiment in Figure 4.10b. We see that in the sawcut sample there are loose grains on the fault surface after the experiment, and that the

surface has become wither and that the fossils are better pronounced. For the waterjet sample, we see that all asperities are broken, but it did not create recoverable gouge with mostly loose grains. Also, the colour changed the least. For the handmade roughness, we see that the asperities are mostly broken, and that the surface has different colours of whiteness.

4.2.3. Mixed samples

In the mixed sample configuration Figure 4.9c, we observed that the mechanical behaviour of the saw-cut configurations is similar, independent of which type of rock is on top. For the waterjet configurations, we see that this does matter and that when the Dinantian carbonate is on top, the stiffness of the sample is lower. We also see that with increasing roughness, the stiffness decreases. This is also visualised in Figure 4.9f. In Figure 4.9i & Figure 4.9l, we also see that with increasing roughness, there is a slight decrease in reactivation stress, and the strain at the reactivation point decreases slighty to a bigger decrease when the Dinantian carbonate is on top.

When we focused on the mechanical behaviour, we observed that the saw-cut samples showed better distinction before and after reactivation compared to the Indiana limestones, but the difference was less clear than in the Dinantian carbonate. The waterjet samples exhibited behaviour more similar to that of the Indiana limestone. In these samples, we observed a gradual change in stress buildup characterised by strain hardening. However, we could not directly distinguish the different phases of reactivation.

In Figure 4.10c, we show the mixed sample configurations for the saw-cut and waterjet. If we look at the post-mortem saw-cut sample 1.1, where the Dinantian was on top of the Indiana limestone. We observe that the faulted surface of the Dinantian is more white because of material from the Indiana limestone. The pattern of this whiteness is located in the direction of striations. On top of the Indiana limestone surface, we do not see any loose grains but better pronunciation of the fossils, and the surface has become more white compared to the situation where we tested Indiana on top of Indiana. When the Indiana limestone was on top (Figure 4.10c 1.2), we see similar things as when the Dinantian carbonate was on top. However, the whiteness on top of the Dinantian surface was less orientated. In the waterjet configuration, we observed similar characteristics for both combinations. We see that on the Dinantian carbonate fault surface, the asperities are still intact and that it is mostly filled with Indiana limestone. On the Indiana limestone, we observe the opposite, as all asperities are broken.

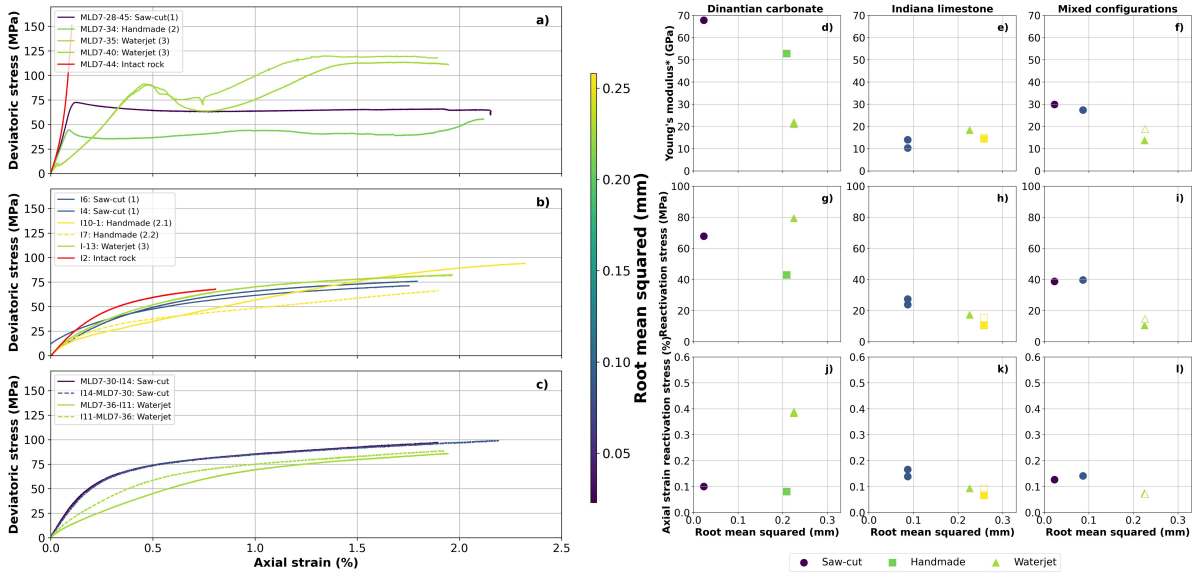

Figure 4.9: The relationship between stress and strain is visualised after hydrostatic conditions ($P_c = 35$ MPa) for the Saw-cut, Handmade, Waterjet, and Intact configurations of a) Dinantian carbonate, b) Indian limestone and c) mixed configurations. Furthermore, the roughness of each profile is characterised by the root mean square, as indicated by the colour bar. In the second part of the graph, the d,e,f) Young's modulus*, g,h,i) reactivation stress and j,k,l) axial strain at reactivation is given for the different lithologies.

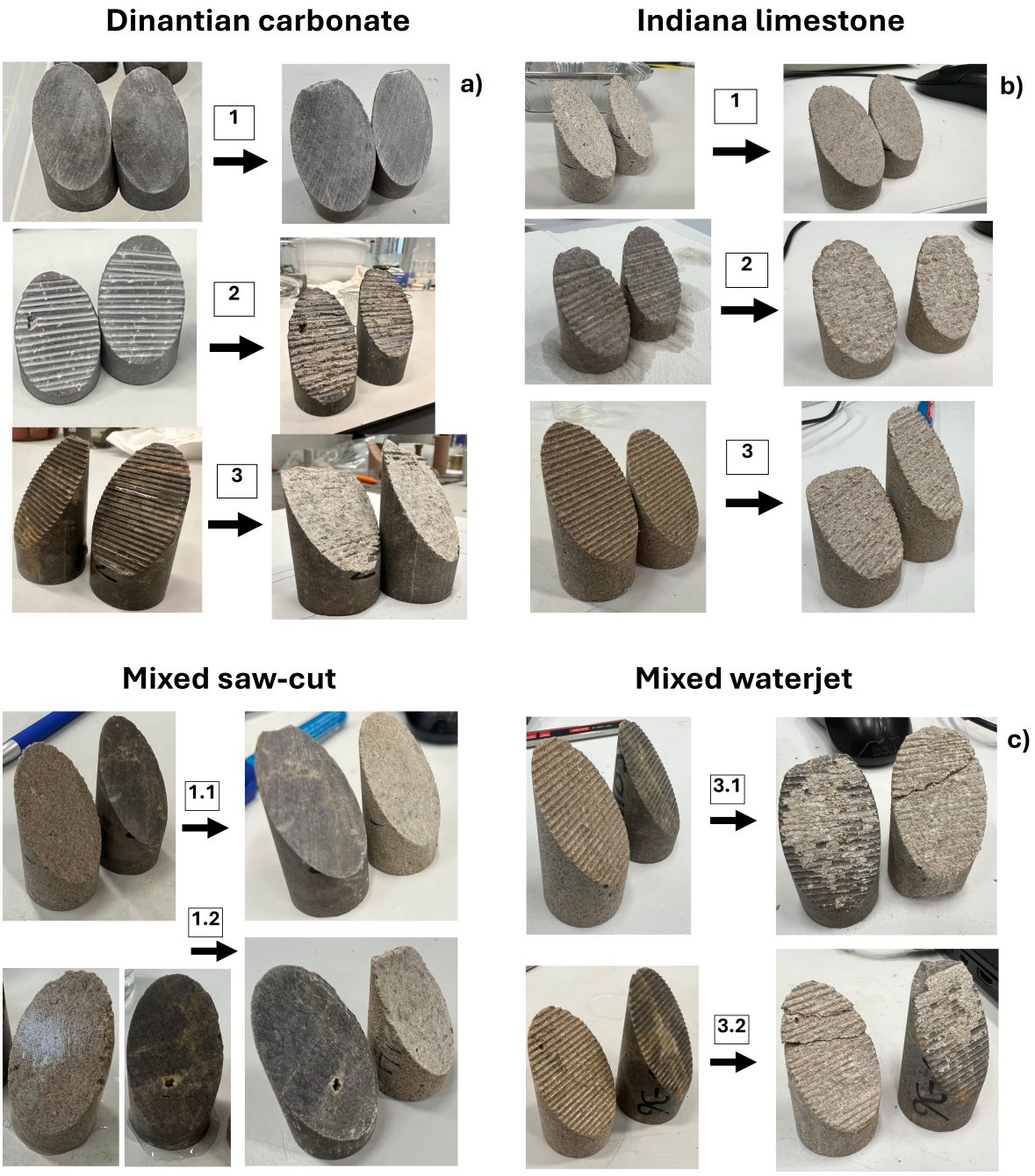

Figure 4.10: Visual representation of surface profiles of a) Dinantian carbonate, b) Indiana limestone and c) mixed samples before and after experimentation: (1) corresponds to the Saw-cut configuration, (2) illustrates the Handmade profile, and (3) represents the Waterjet roughness profile. For the mixed samples, a suffix of .1 indicates that the Dinantian carbonate was positioned on top, whereas .2 indicates that the Indiana limestone was on top.

Sorted on roughness

From Figure 4.11, we observe that in the saw-cut experiments (a), there is a decrease in reactivation stress and stiffness going from the Diantian to the Indiana limestone samples. The mixed configuration falls between these values. In the handmade experiments (b), we see that reactivation does happen with less stress for the Indiana limestone compared to the Dinantian. Additionally, the sample stiffness is lower for the Indiana limestone compared to the Dinantian limestone. In the waterjet experiments (c), we observe that the stiffness of the samples is within a similar range, especially at the start of

the experiment. We observe that the yield point is highest for the Dinantian and lowest for the mixed samples, followed closely by the Indiana limestone.

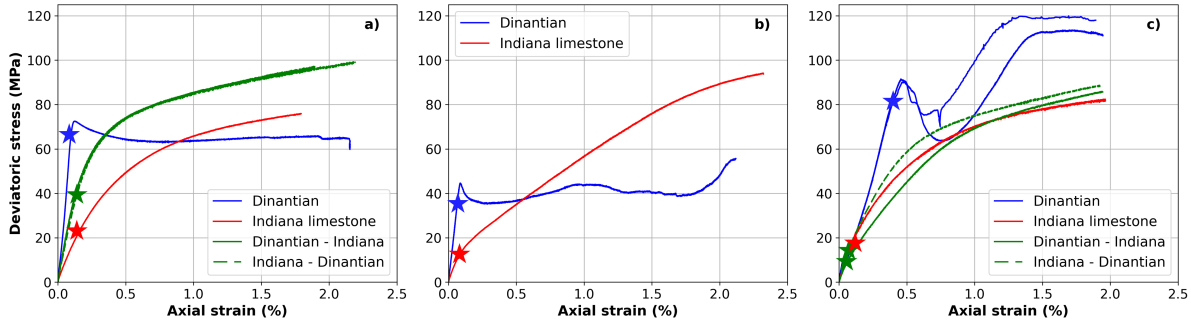

Figure 4.11: The relationship between stress and strain is visualised after hydrostatic conditions ($P_c = 35$ MPa) for Dinantian carbonate, Indiana Limestone and mixed samples. This plot is categorised based on the roughness profiles. Plot a) visualises the Saw-cut roughness, b) the Handmade roughness and c) the Waterjet roughness. In this plot, the stars indicate reactivation of the laboratory fault.

4.3. Injection-driven fault reactivation: saw-cut roughness

In addition to the displacement-driven experiments, we performed injection experiments on critically stressed saw-cut samples as described in section 3.2. Here we test each configuration once. We present the results in Figure 4.12. Here, it's important to note that delta pressure over the pipes is measured with a separate sensor close to the sample. However, we also included the difference between the two pumps as the delta pressure sensor has a maximum value of 1.7 MPa. From the sample post-mortem, we did not obtain any clear deformation mechanics as in the displacement-driven experiments. Additionally, we also did a permeability test on the Indiana limestone. We performed these experiments at a confining pressure of 35 MPa.

In Figure 5.7a we visualise how the axial stress and pore pressure have been built up in the Dinantian carbonate. The graph demonstrates a pressure difference across the sample, with pump A exhibiting higher pressure than pump B. This implies that the fluid flow encounters resistance along its path. Additionally, we see reactivation happening at point b. The corresponding reactivation pressures for pump A is 5.15 MPa and 1.78 MPa for pump B.

From Figure 5.7b, we visualise the same protocol but applied to the Indiana limestone. Here, we see that the pumps A and B have similar pressures, indicating constant flow. The reactivation pressure for pump A was 23.82 MPa and 23.94 MPa for pump B.

In Figure 5.7c & 5.7d we see the results for the mixed sample configurations. Here we observe that when the Indiana limestone is on the bottom of the sample, dP is bigger than when the Dinantian carbonate is on the bottom. This results in a reactivation pressure for Pump A and B of 23.13 MPa, 21.14 MPa when the Dinantian carbonate is on top and 20.32 MPa and 20.2 MPa when the Indiana limestone is on top.

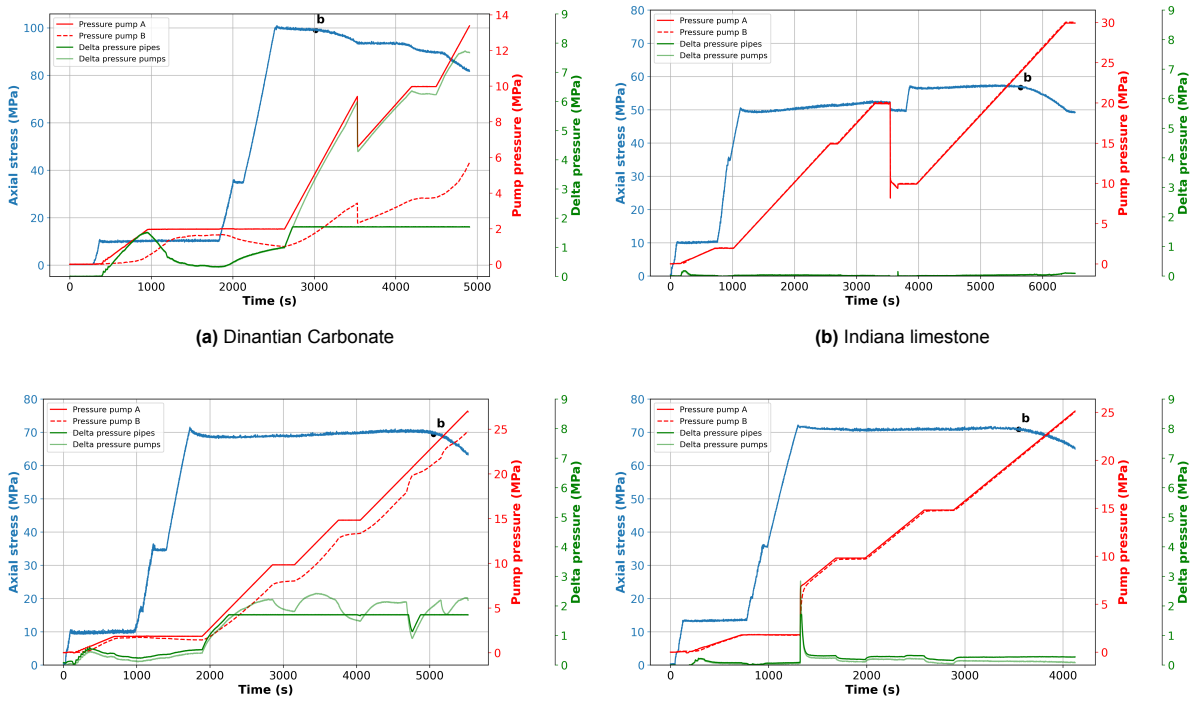

(a) Dinantian Carbonate

(b) Indiana limestone

(c) Dinantian carbonate on top of Indiana limestone

(d) Indiana limestone on top of Dinantian carbonate

Figure 4.12: Evolution of axial stress and pressure of pump A and B over time, with their delta pressure measured at the pump and over the pipes closer to the samples. a) Dinantian carbonate sample, b) Indiana limestone, c) Dinantian carbonate on top of Indiana limestone and d) Indiana limestone on top of Dinantian carbonate. Point b indicates the reactivation caused by pore pressure.

4.3.1. Permeability test Indiana limestone

In the series of injection experiments, we also perform one permeability test on the Indiana limestone at 10 MPa. Here, we test three different flow rates until it reaches a steady state to determine the permeability as described in section 2.5.

In Figure 4.13, we select one point where ”steady state” is reached during each flow cycle. Based on the flow rate and delta pressure, we can calculate three times the permeability based on Equation 2.22. In the first run, a permeability of 8.4 mD is calculated, in the second run, a permeability of 10.4 mD and in the last run, a permeability of 10.5 mD. Before the experiments, we also measured the Tiny permeability of these samples. The average Tiny permeability is 12.04, which is equivalent to 10.37 mD. Therefore, the Tiny permeability gives a good representation of the permeability obtained from testing.

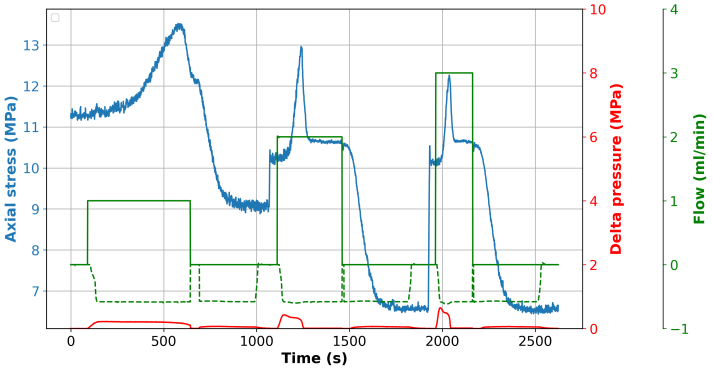

Figure 4.13: Evolution of axial stress, delta pressure and flow over time in the permeability test on the Indiana limestone.

5 Discussion

5.1. Displacement-driven fault reactivation

In this section, we will analyse the Mohr-Coulomb stresses (as described in section 2.3) based on roughness and lithology, along with their corresponding shearing behaviour. Then, we will discuss the effect of roughness on matrix versus fault deformation, while examining the different configurations. Additionally, we assume that the contact fault area is constant and does not slip. Hence, the stress distribution along the fault is not time-dependent. In the displacement-driven fault reactivation experiments, we control the axial stress applied to the top of the sample and the confining stress in the radial direction. Therefore, we cannot directly control the normal and shear stresses acting on the fault.

5.1.1. Mohr-Coulomb anysis

Effect of roughness

In Figure 5.1, we visualise the critical stresses based on the Mohr-Coulomb failure criteria sorted on lithology. For the Dinantian samples, we observed that fault roughness, quantified with RMS, did not correlate with the Mohr-Coulomb critical stresses. We observed that going from the saw-cut sample (RMS = 0.023) to the waterjet sample (RMS = 0.225), there was an increase in Mohr-Coulomb stresses. However, from the saw-cut to the handmade (RMS = 0.209), critical stresses decreased. For the Indiana limestone and mixed samples, the RMS of fault roughness negatively correlated with the Mohr-Coulomb stresses. Therefore, fault roughness negatively correlates with critical stresses for the less compliant rock types. To our knowledge, no literature has captured a similar effect.

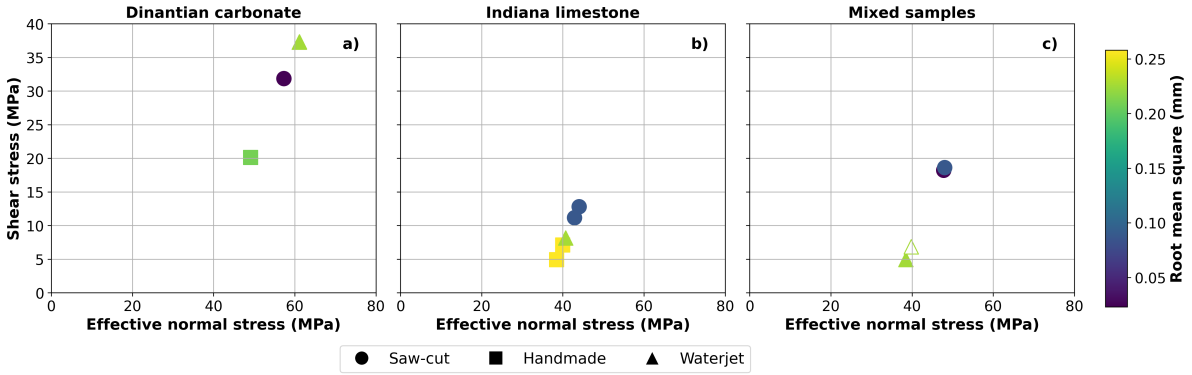

Figure 5.1: The relationship between the effective normal stress and shear stress based on the reactivation point using Mohr-Coulomb. Here, we sort the points based on lithology. The colour bar indicates the Root mean square used to distinguish between the roughness profiles.

Effect of fault and rock deformation (system stiffness) versus rock deformation (matrix stiffness) on Mohr-Coulomb stresses

Figure 5.2 presents the effect of the stiffness of the system (matrix and fault) on the critical stresses clustered by roughness type. We observed that the system stiffness positively correlated with the critical stresses for the saw-cut, waterjet and handmade roughness. Therefore, we suggest that the Young's modulus* of the fault and matrix is an influencing parameter for all roughness configurations. For the Dinantian carbonate, this results in the highest critical stress in each surface roughness configuration. Notably, the mixed samples in the saw-cut configuration exhibited an intermediate mechanical stress-strain behaviour, leaning towards the more compliant member. In the waterjet configuration, the mixed samples tend towards the lowest reactivation stresses.

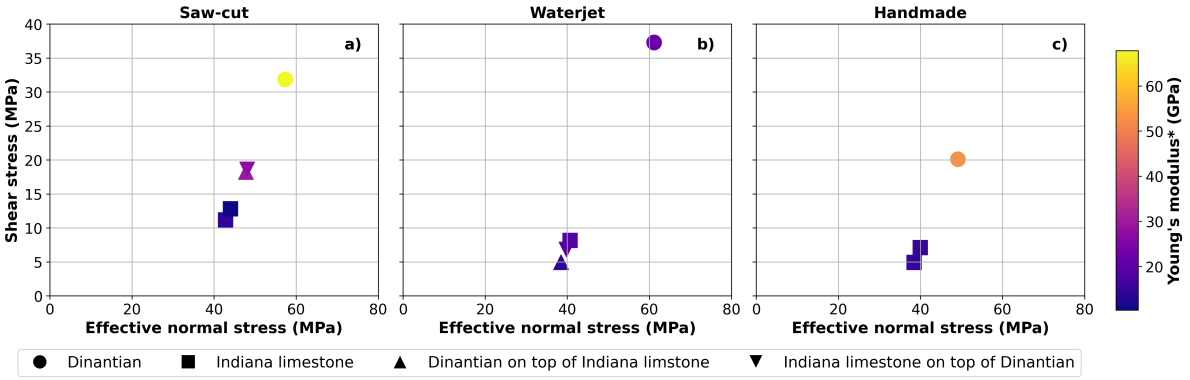

Figure 5.2: The relationship between the effective normal stress and shear stress based on the reactivation point using Mohr-Coulomb. Here, we sort the points based on roughness. The colour bar indicates the Young's modulus* of the sample.

To further investigate the effect of lithology, we can also link the reactivation to the properties of intact rock. As it seems that the more compliant rock is the influencing factor, we will use the mechanical properties of the compliant member in the mixed configurations. From Figure 5.3, we observe that in both UCS and triaxial experiments, the peak stress, yield point, and Young's modulus correlate negatively with porosity. Therefore, we can use this relation to distinguish between the matrix rock properties of the Dinantian carbonate and Indiana limestone in both UCS and triaxial experiments.

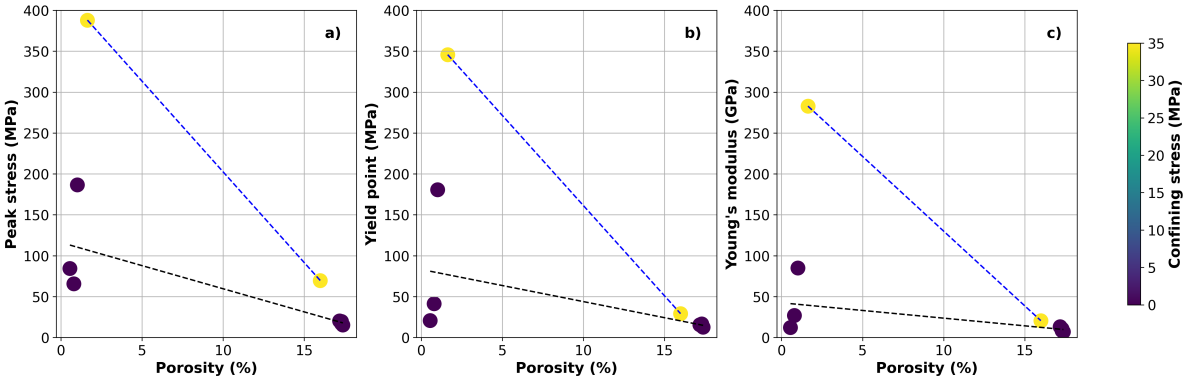

Figure 5.3

In Figure 5.4a and Figure 5.4b, we see that the intact rock properties of the UCS and triaxial experiments correlate positively with the reactivation stresses for all roughness configurations. Therefore, matrix properties of the intact rock seem to govern the reaction behaviour as well. In our initial analysis (Figure 5.2), we showed that both fault and matrix stiffness have a clear positive correlation with the Mohr-Coulomb reactivation stress. However, matrix stiffness plays a vital role on its own as well.

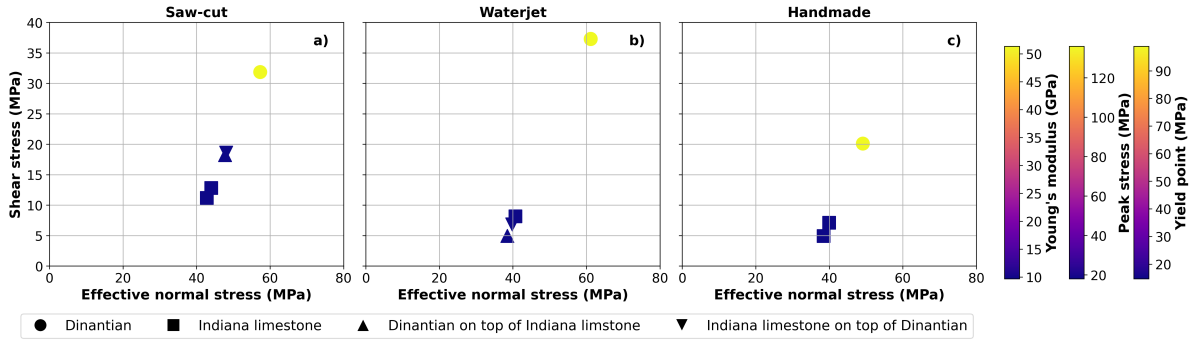

(a) The relationship between the effective normal stress and shear stress based on the reactivation point using Mohr-Coulomb. Here, we sort the points based on roughness. The colour bar indicates the intact rock properties of UCS experiments.

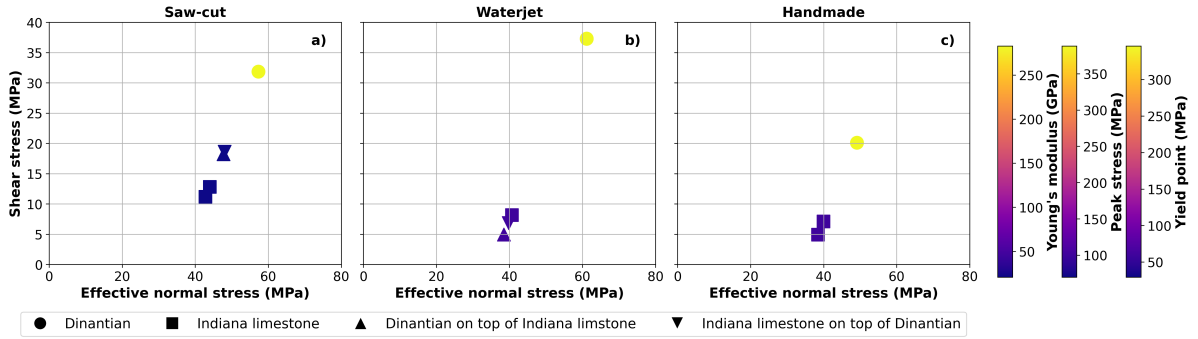

(b) The relationship between the effective normal stress and shear stress based on the reactivation point using Mohr-Coulomb. Here, we sort the points based on roughness. The colour bar indicates the intact rock properties from the triaxial experiments.

Figure 5.4: Mohr-Coulomb reactivation stress sorted on roughness and characterised based on Young's modulus, peak stress and yield point of intact rocks

Shearing behaviour

From the normal stress and shear stress, we can also compute the dynamic friction. In Figure 5.5 we visualise the dynamic friction after hydrostatic conditions for all saw-cut, waterjet and handmade samples. The waterjet and handmade samples are characterised by a higher RMS and the saw-cut samples by a lower one.

For the Dinantian carbonate, we observe that the dynamic friction coefficient builds up quickly in the saw-cut sample. After reactivation, it increases slightly, after which it reaches a steady state. For the waterjet, we see that this build-up is slower but reaches higher values due to the interlocking of the asperities. For the handmade, we observe the same buildup as in the saw-cut, but with early reactivation and the effect of stick-slip in the after-shearing behaviour. In the Indiana limestone, we observe that the buildup is relatively similar and starts to deviate after reactivation. In the mixed samples, we observe the effect of roughness, as the saw-cut samples have a higher friction coefficient than the waterjet samples. This may result from the breakdown of asperities in the Indiana limestone and the subsequent smearing of the material across the Dinantian carbonate surface. In general, we observe that the Dinantian carbonate exhibits a higher dynamic friction coefficient during reactivation. The Indiana limestone samples have the lowest values, and the mixed samples fall in between.

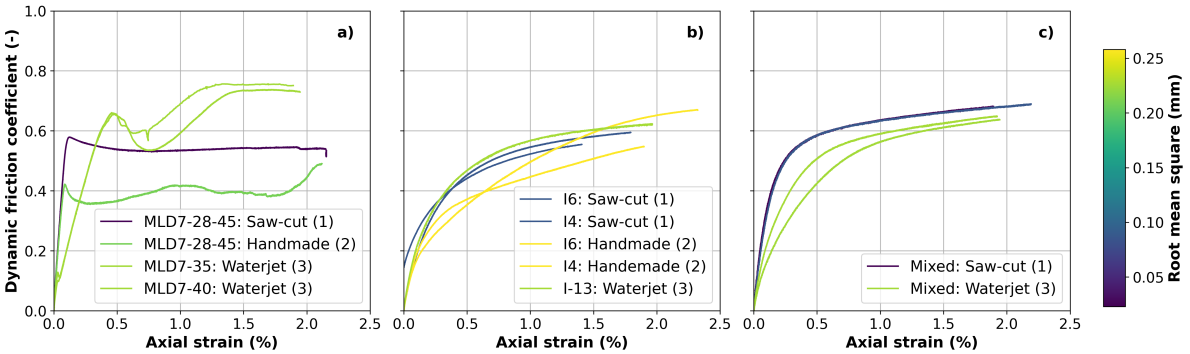

Figure 5.5: The relationship between dynamic friction and axial strain is illustrated for all samples. Saw-cut profiles(1), characterised by a lower RMS, are compared with handmade and waterjet-cut profiles with higher RMS. Axial strain has been normalised for the onset of deviatoric loading, following hydrostatic conditions.

5.1.2. Effect of roughness on rock and fault deformation

Dinantian carbonate

The stiffness of Dinantian samples is the highest among all the samples; hence, the matrix itself accommodates minimal deformation until failure occurs, either through the development of a shear fracture under confined conditions or via axial splitting in UCS tests. Additionally, the effect of rock-fluid interaction, as determined by the UCS tests (DI water vs. brine), had a limited impact on the unconfined mechanical strength. However, we did not investigate the effect of rock-fluid interaction under triaxial conditions. Therefore, we used DI water as an approximation of the in situ fluid conditions due to ample availability, although brine would be more realistic.

In the Dinantian carbonate saw-cut experiment, fault reactivation occurred at a deviatoric stress of 68 MPa, corresponding to an axial strain of 0.1%. We suggest that the fault zone accommodated most of the strain, given the stiff matrix of the sample. Fault reactivation was triggered when the applied stress exceeded the shear strength of the relatively smooth fault surface. After reactivation, we observed constant sliding, which we confirmed by the visual observation of lineations (Figure 4.10a.1)(i.e., top surface is scratched permanently in a brittle way).

In the Dinantian carbonate waterjet samples, we increased the fault zone thickness by the amplitude of the asperities. Here, we observed that reactivation occurred at a deviatoric stress of 79 MPa, accompanied by approximately 0.4% axial strain. We observed that substantial strain is accommodated in the fault zone before reactivation. We speculate that the interlocking of asperities and deformation of these asperities upon reactivation yield high strain. Once they interlocked again, the fault zone was deformed until all asperities were broken. Then the fault zone started to behave like a saw-cut sample. The visual observations confirm this, as the fault zone is completely broken (Figure 4.10a.3).

In the handmade variant, we observed reactivation at stresses of 43 MPa, with a comparable amount of strain to that of the saw-cut. We suggest that the early reactivation stems from the irregularity of the asperities that do not interlock. Only after reactivation did we observe minor stress buildup, which provided evidence of asperity interlocking. In the visual observation, we could visually inspect that the tips of the asperities were minimally damaged (Figure 4.10a.2).

Indiana limestone

Here we apply the same analysis to the Indiana limestone samples. From our triaxial experiments on intact rocks, we observed the strain hardening behaviour post-yielding of the matrix. In literature, the same behaviour is described as a result of confining stress. For the Indiana limestone, there is a well-described transition zone between 20 to 30 MPa of confining stress where its behaviour changes from brittle to ductile deformation (Walton et al., 2017). This implies that the matrix behaves in a compliant manner and exhibits compaction.

In the saw-cut configuration of the Indiana limestone, both the matrix and the fault zone are active. We observe that the behaviour is very similar to that of the intact sample; however, now strain is also accommodated within the fault zone. Fault reactivation occurred at a deviatoric stress of around 24

MPa with around 0.18 % of axial strain. During the sliding phase, deformation localises along the fault plane. Post-mortem visual observations reveal a polished slip surface characterised by a lighter colouration and more distinct expression of the fossil (Figure 4.10b.1). These attributes are indicative of frictional wear associated with brittle-frictional deformation mechanisms (Cilona et al., 2012).

For the waterjet sample, we observe a similar behaviour of the matrix. However, reactivation now occurs at a deviatoric stress of 17 MPa with approximately 0.1% axial strain. At this stage, the fault zone demonstrates limited capacity to accommodate additional strain. The asperities fail relatively easily when the stress distribution is higher in the fault zone. Upon failure, all asperities are broken and subsequently smeared across the fault surface. This process results in the formation of loose grains, interpreted as gouge material, distributed across the reactivated zone. Visual observations confirm this (Figure 4.10b.3). Notably, the absence of a secondary stress build-up suggests that asperity failure occurs entirely during the initial reactivation. The stress–strain response remains influenced by the matrix.

In the Handmade variant, matrix behaviour is also visible. Here we tested two types of handmade roughness. One had around 16 groves while the other had around 4 groves. Despite this difference, the fault starts to slide at around 10 MPa of deviatoric stress, accompanied by approximately 0.1% axial strain. This seems to be a result of the fact that the asperities do not interlock with each other. At the fault surface, we see that the fault surface is smeared into the grooves while sliding. When a higher number of grooves is present, this smearing occurs more irregularly, likely due to the increased complexity of the fault surface (Figure 4.10b.2).

Mixed samples

In the mixed saw-cut experiments, fault reactivation occurs at approximately 40 MPa of deviatoric stress and around 0.13% axial strain. Notably, the sequence in which rocks are stacked does not matter for the mechanical response. Before reactivation, the strain appears to be localised more within the fault zone rather than in the matrix. However, following reactivation, the mechanical response seems to be predominantly governed by the matrix of the Indiana Limestone. Post-mortem observations of the fault surface reveal that, in both configurations, the Indiana Limestone is smeared across the Dinantian surface, with evidence of frictional polishing (Figure 4.10b.1). This indicates that although the Dinantian contributes to the stiffness of the system, it is not actively deformed.

When asperities are introduced, fault reactivation is influenced by the relative position of the lithologies. When the Dinantian is positioned on top, reactivation occurs at a deviatoric stress of approximately 10 MPa, with axial strain greater than 0.09%. This indicates that the fault does not accommodate a lot of strain, and the apertures break easily, after which slip occurs and the mechanical response becomes increasingly influenced by matrix compaction of the Indiana limestone. Post-mortem observations reveal that all Indiana Limestone asperities are broken and that it is smeared over all the asperities. Here, the gouge material is spread more than in the configuration where the Indiana is on top (Figure 4.10b.3.1). This indicates that more sliding did occur.

In contrast, when the Indiana Limestone is placed on top, fault reactivation occurs at a higher deviatoric stress of approximately 15 MPa and an axial strain of around 0.09%. This suggests that when the Dinantian pushes into the Indiana Limestone, the asperities fail less easily but accommodate a similar amount of deformation. Post-mortem inspection confirms that the Indiana Limestone has been smeared into the Dinantian surface (Figure 4.10b.3.2). After reactivation, the mechanical behaviour is once again influenced by matrix compaction of the Indiana Limestone.

Saw-cut versus waterjet samples

Dinantian carbonate

Our Mohr-Coulomb analysis indicates that for the saw-cut and waterjet configurations, roughness appears to be a significant factor in determining the reactivation stress. However, the effective normal and shear stresses are within the range of each other if you consider experimental variability for the saw-cut experiments. The waterjet experiment has been consistently proven. The primary difference between the two roughness profiles lies in the amount of strain that can be accommodated before reactivation. In the waterjet samples, reactivation occurs after a higher amount of axial strain compared to the saw-cut configuration. This suggests that deformation is more distributed within the fault zone before reactivation in the presence of a rougher surface.

This difference can be attributed to the presence of interlocking asperities in the waterjet samples. Before slip initiates, these asperities are progressively crumpled, allowing the fault zone to deform locally while resisting slip. This deformation mechanism delays reactivation, resulting in a higher axial stress and a dynamic friction threshold that is more difficult to overcome due to mechanical interlocking, despite relatively similar normal and shear stresses. Post-mortem analysis confirms that the asperities in the waterjet samples are completely broken, whereas the saw-cut samples show lineations on continuous slip surfaces. This aligns with outcrop observations in low-carbonate rocks where deformation is predominantly brittle and localised depending on geometry (Bastesen and Braathen, 2010). In other words, we can infer that after the experiment, the fault zone has matured into asperities where the broken material is concentrated, and the fault surface has become smoother in the slip-parallel direction (Sagy, Brodsky, and Axen, 2007; Candela et al., 2012).

Once the asperities are destroyed, the waterjet samples begin to slide like the saw-cut configuration. However, this sliding is caused by a higher steady-state friction in the waterjet samples. This could be due to the additional resistance introduced by the gouge. The higher frictional resistance during sliding and the greater strain accommodated before reactivation, together, indicate that roughness influences fault mechanics by modifying how strain localises and how failure progresses at the fault zone.

Indiana limestone

In the Indiana limestone, the Mohr-Coulomb analysis indicates that roughness decreases the amount of normal and shear stress to reactivate the fault zone. This suggests that roughness may play a more significant role in influencing the stress state compared to the Dinantian carbonate. However, matrix properties of the Indiana limestone do significantly affect mechanical behaviour. Making it hard to isolate the effect of fault roughness alone. In literature, it is described that compaction is an influencing factor at both the microscale and the outcrop scale, as observed here (Delle Piane et al., 2017; Cilona et al., 2012).

By adding asperities to the fault surface, we observe that the stiffness of both the matrix and the fault increases. However, for a short period, reactivation needed less stress and could accommodate less strain. This implies that the stress distribution in the fault zone can break asperities more easily (Post-mortem observations confirm this). This indicates that adding roughness weakens the fault plane for the Indiana limestone. Despite the presence of gouge, the increase in the friction coefficient in the waterjet samples is only slight compared to the saw-cut configuration. This suggests that roughness is not the primary factor, and the compaction of the matrix primarily governs the mechanical response.

After reactivation, deformation is dominated by matrix compaction. From the evolution of the friction coefficient, we see that there is no steady-state slip. Nevertheless, post-mortem observation does show signs of slip along the fault plane.

Mixed samples

In the mixed configuration, we observe distinct mechanical behaviours depending on the roughness. The Mohr-Coulomb analysis indicates that with higher roughness, the amount of normal and shear stress required to reactivate is lower. Indicating that roughness facilitates fault reactivation, similar to the Iniana limestone. From post-mortem observation, we observe smearing of the Indiana limestone over the intact Dinantian carbonate in the saw-cut and waterjet. Increasing the amplitude of the asperities in the Indiana limestone promotes early reactivation by localising stress and initiating gouge formation. This production of gouge appears to lubricate the fault, as evidenced by a lower dynamic friction coefficient in the mixed samples. To our knowledge, the literature does not directly describe this lubrication effect by limestone gouge at room temperature. There is supporting evidence that captured fault lubrication in a rotary shear experiment subjected to an increase in temperature (Di Toro et al., 2011).

Therefore, we imply that in displacement-driven conditions, heterogeneous fault reactivation is influenced by the stress distribution on the fault. In case stress is uniformly distributed along the fault, pre-reactivation behaviour is primarily governed by the stiff lithology. However, more strain is accommodated in the compliant member. In contrast, post-reactivation behaviour is increasingly dominated by the compliant lithology, indicating the significant effect of matrix deformation. When the stress distribution across the fault zone is heterogeneously distributed, both pre- and post-reactivation are dom-

inated by the compliant lithology. Less deformation is accommodated as only the compliant lithology will deform, and asperities are broken more easily by the stiff lithology.

Here, it is essential to note that determining the reactivation stress from the stress-strain curves of the waterjet experiments proved to be difficult. To improve this analysis and better pick this point, the acoustic emission recording can be used.

5.2. Injection-driven fault reactivation

As with the displacement-driven experiments, we calculate the reactivation stresses based on the Mohr-Coulomb criterion, now incorporating the effect of pore pressure (assuming a Biot coefficient of 1). The methodology is outlined in section 2.3. We present the reactivation stresses and starting points for the injection experiments in in Figure 5.6. Pore pressure reduces the effective normal stress, and the shear stress only changes marginally. The results indicate that the Dinantian carbonate exhibited the highest critical stress, accompanied by the lowest pore pressure. In contrast, the Indiana limestone demonstrated the lowest critical stress under the highest pore pressure. As a result of the protocol used during the Indiana limestone experiment, we see that the difference between the starting point and the critical point is not 24 MPa. This is because at the starting point, there was already 10 MPa of pore pressure in the system. Nevertheless, the absolute value of the critical pore pressure was 24 MPa.

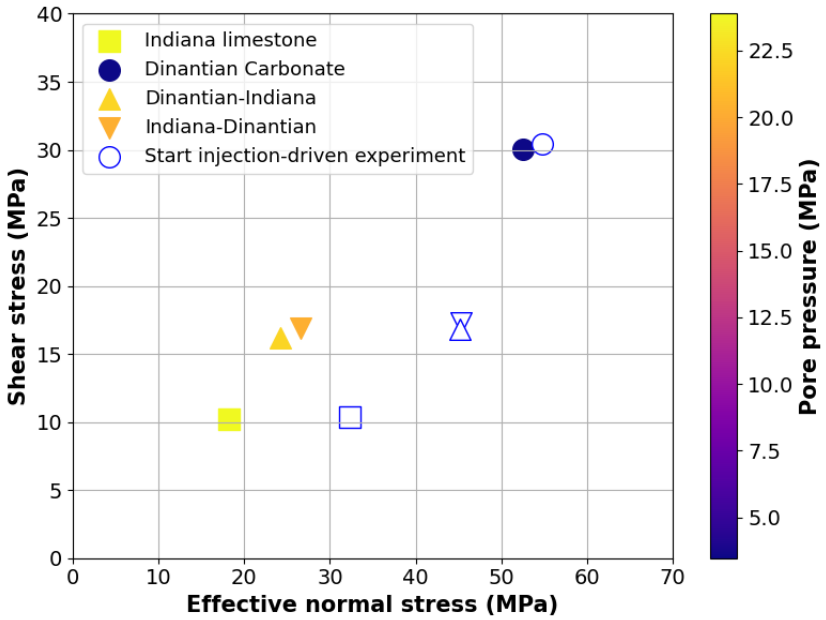

Figure 5.6: Reactivation shear stress and effective normal stress for different lithologies in injection-driven saw-cut experiments. The colour bar indicates the Young's modulus of the sample configuration.

In the injection experiments, we tested matrix flow and fracture flow in the saw-cut samples. From Figure 5.6 we observed that in the case of matrix flow in the Indiana limestone, a critical pore pressure of 24 MPa was needed to reactivate, but in the case of fracture flow in the Dinantian carbonate, only 3.5 MPa was needed. To elaborate on this effect, Figure 5.7 gives a schematic representation of how the pore pressure is introduced to the sample. To induce flow in the Dinantian carbonate, a hole has been drilled without compromising its strength (Li and A. M. Pluymakers, 2024).

We observed in Diantian carbonate samples (Figure 5.7a) that the back pressure did not follow the injection pressure. This indicates that the fluid path had some resistance due to limited permeability. At the fault zone, we induce a local increase in pore pressure that tends to open the fault plane. This effect seems to result in early reactivation with only 3.5 MPa of pore pressure. In contrast, the Indiana limestone sample (Figure 5.7b) exhibited no significant pressure difference between the pumps, indicating that matrix flow allowed a more uniform pressure distribution over the sample. Consequently, a

higher pore pressure of 24 MPa yielded the reactivation of the fault.

When the Dinantian carbonate is on top Figure 5.7c, we observed a pressure difference between pump A and B, and we interpret this to be the resistance of flow between the top middle of the sample and the piston towards the side. The critical pore pressure was 22 MPa. Conversely, when the Indiana limestone was placed on top, we did not observe a pressure difference between pump A and B. Reactivation occurred at a pore pressure of around 20 MPa. We speculate that the type of flow of the bottom block causes the observed differences in reactivation behaviour in the mixed samples. When the Indiana limestone is on the bottom, stress seems to be more evenly distributed across the fault plane. However, when the Dinantian carbonate is at the bottom, stress localisation is more pronounced by fracture flow towards the fault.

Overall, a distinction is observed between the reactivation behaviour of the Dinantian carbonate, which reactivates under relatively low pore pressure, and the other samples, which require higher pore pressures. This difference appears to result from localised pressure build-up along the fault plane in the Dinantian sample, as opposed to more uniformly distributed pore pressure in the others.

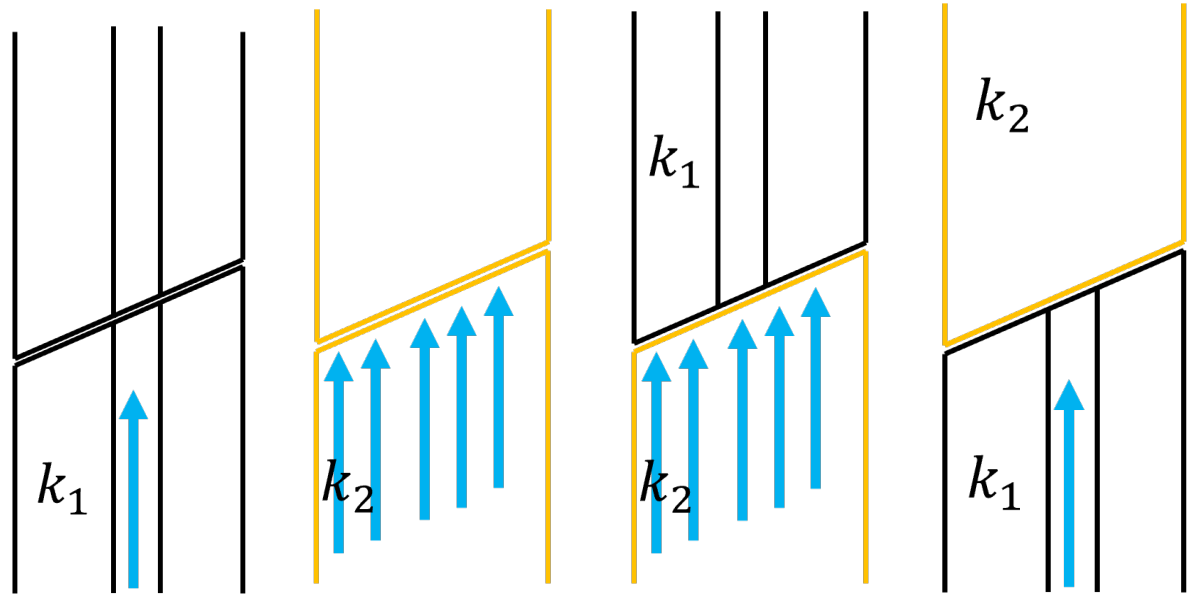

(a) Dinantian carbonate **(b)** Indiana limestone **(c)** Dinantian on Indiana **(d)** Indiana on Dinantian

Figure 5.7: Schematic representation of the types of flow towards the fault in the injection experiments. It is important to note that during the experiments, the fault zones are touching each other.

5.3. Comparison of displacement-driven and injection-driven fault reactivation

In Figure 5.8 we visualise the critical stress for the displacement-driven experiments and injection-driven fault reactivation experiments of the saw-cut configurations. We also plot the starting point of the effective normal and shear stresses on the fault. We assume that for pre-existing fault cohesion approximates 0 (Byerlee, 1978) at lower stresses. In this scenario, we expect that critically stressed faults reactivate with a minimal contribution of pore pressure.

In the Dinantian carbonate, we see that a minimal pore pressure induces fault reactivation, the lowest among all configurations. Hence, the critical points overlap. Indiana limestone requires a substantial pore pressure for reactivation, which is higher than that of the Dinantian sample. Therefore, the injection-driven critical point exhibits lower Mohr-Coulomb stresses than the displacement-driven. The difference implies the effect of a homogeneous increase of pressure distribution in the sample and fault zone, resulting in a lower effective normal stress to overcome the shear stress. In our permeability test at a confining pressure of 10 MPa, we also reactivated the sample. This gives us an additional point on the Mohr-Coulomb stresses. Considering the confining pressure of 10 MPa, a considerable amount

of pore pressure was also needed to reactivate the sample supporting the finings at 35 MPa. In the mixed samples, a pore pressure of 20 to 22 MPa was required to reactivate the sample. Hence, the injection-driven critical stress is lower than in the displacement-driven experiments. This behaviour tends towards what was observed in the Indiana limestone. This implies that when matrix and fracture flow are combined at the fault, matrix flow dominates in the distribution of pressure in the fault zone. This results in a lower effective normal stress to overcome the shear stress.

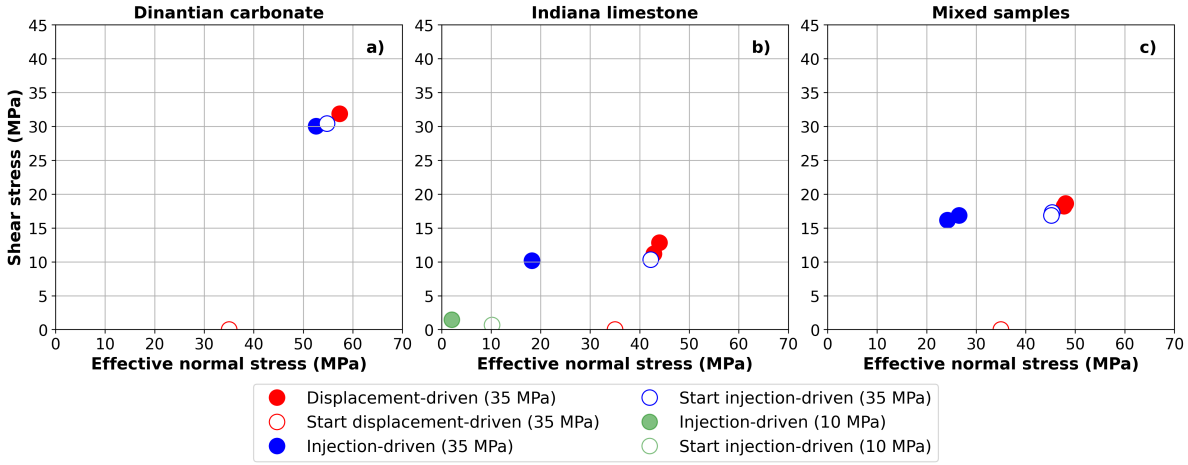

Figure 5.8: Displacement and injection-driven experiment on Mohr-Coulomb failure diagram.

In our experimental work, it becomes clear that lithological heterogeneities play a critical role in controlling fault reactivation. While porosity correlates negatively with the elastic moduli and peak stress of the intact rock in both confined and unconfined conditions, we see that this relation weakens in faulted experiments. In our low porosity Dinantian carbonates samples, which exhibit the highest system and matrix stiffness, the critical stress is the highest. However, in injection-driven conditions, their low porosity results in the need for fracture flow, which enables localised pore pressure accumulation. Hence, the lowest reactivation pore pressure. Conversely, in the more compliant lithologies, such as Indiana limestone, with higher porosity, lower critical stresses are observed. However, in injection-driven conditions, more pore pressure can accumulate. For the mixed samples, we observe an intermediate behaviour in terms of critical reaction stress, tending towards the weaker lithology, with the ability to accumulate pore pressure in injection-driven conditions. This indicates that fault reactivation is sensitive to the distribution of mechanical properties along the fault, particularly in terms of stiffness contrasts and the localisation of strain before slip. This implies that porosity alone cannot explain these effects. Therefore, we see the importance of lithology stiffness, local permeability and deformation style (matrix versus fault-dominated)

5.4. Implications for induced seismicity

Understanding the effect of normal stresses on fault reactivation is the first step to understanding induced seismicity. The displacement-driven experiments mimic a form of more natural seismicity where horizontal/vertical stresses are perturbed, while the injection experiments simulate induced seismicity. The observed behaviour in our displacement-driven and injection experiments gives critical insight into what governs fault reactivation in the subsurface in potential carbonate reservoirs. In our injection experiments, we gained insights into the effect of juxtaposition and matrix versus fracture flow for induced seismicity.

The injection experiments on the Dinantian carbonate and Indiana limestone highlight the contrasting effects of fracture versus matrixial flow in controlling the distribution of pore pressure over the sample, or on a bigger scale, the reservoir. Fracture flow in the Dinantian carbonate leads to a localised pressure distribution on the fault. Additionally, displacement-driven experiments learned us that within the Dinantian carbonate samples, most of the deformation is localised in the fault zone. This behaviour is due to the high matrix stiffness of the rock, which yields the highest critical stresses. The combination

of localised deformation and fracture flow most likely results in reactivation with low pore pressure. This more abrupt transition to slip increases the likelihood of seismic slip events that can release significant energy. This implies that in low-porosity faulted carbonate reservoirs characterised by fracture flow, there is a high risk of induced seismicity. This aligns with the field-scale observations where seismic events have been captured in fractured low-porosity carbonates (Seithel et al., 2019; Diehl et al., 2017; Buijze et al., 2019).

In a matrix flow-dominated system, we observed that a higher pore pressure is required to reactivate the fault. Here, the stress distribution was likely more evenly distributed across the fault. This could translate on a bigger scale to less seismically hazardous conditions. This is supported by the absence of induced seismicity in carbonate rocks that do not rely on fracture flow. Additionally, from the displacement-driven experiments, we learned that in Indiana limestone, both the matrix and the fault accommodate deformation. Here, matrix compaction was the primary influence on the mechanical behaviour, which is a common feature in porous carbonate fault zones (Delle Piane et al., 2017; Rotevatn et al., 2016).

In our juxtaposition experiments, we observed the potential effect of contrast in porosity at a fault zone in a reservoir. Depending on the type of flow in the bottom lithology, the stress is distributed slightly differently. However, this results in somewhat similar effective normal stress and shear stress. We observed that in mature juxtaposition faults, reactivation is dependent on the stiffness of the more compliant member. This implies that contrast in mechanical properties results in behaviours depending on the more compliant lithology.

Overall, induced seismicity appears to be a higher risk in a critically stressed fault zone with less porous carbonate rock that exhibits secondary permeability in the form of fractures.

6

Conclusion

The goal of this study was to investigate the geomechanical behaviour of heterogeneous laboratory carbonate faults. Therefore, we performed UCS and triaxial experiments to understand the mechanical behaviour of intact carbonate rocks. Then, displacement and injection-driven experiments were conducted to capture the effect of laboratory carbonate faults. Heterogeneity is created by mixing lithologies and different stress distributions on the fault due to roughness. The research question can be answered as follows.

- What are the implications of variations in mechanical properties for laboratory fault reactivation and shearing behaviour? How does this relate to the Mohr-Coulomb stress on the fault at reactivation?
  For smooth (low RMS) laboratory fault reactivation, we observed that variation in mechanical properties results in a pre-reactivation behaviour that is still dominated by the stiff member and a post-reactivation behaviour in which the compliant member dominates. On the Mohr-Coulomb stresses, we see that reactivation stresses tend towards the compliant lithology. For rougher (high RMS) faults, we see that the compliant lithology dominates the pre- and post-mechanical behaviour. The Mohr-Coulomb stresses drop below that of the compliant member and therefore stimulate reactivation. In general, reactivation is dependent on the Young's modulus of the system, which is influenced by matrix stiffness.
- How does fault roughness affect the reactivation of laboratory faults? How does this relate to the mechanical properties of the rock?
  Depending on the lithology, roughness influences the reactivation of laboratory faults. In stiffer members, no direct link was found between the RMS roughness and the reactivation stresses. However, reactivation depends on the interlocking of the asperities. In case of the highest reactivation stress on the fault, the asperities were able to interlock, whereas the lowest reactivation stress did not stimulate interlocking. In a more compliant lithology or a mixed lithology, roughness seems to influence reactivation. Higher roughness seems to stimulate reactivation in lithologies with a lower stiffness and UCS.
- What is the effect of pore pressure on the reactivation of critically stressed laboratory faults? What is the influence of the mechanical properties?
  The effect of pore pressure in critically stressed faults depends on the type of flow and matrix properties of the rock. Low-porosity carbonate rocks that rely on fracture flow tend to reactivate with significantly less pore pressure compared to porous carbonates that have matrix flow. This is the effect of pore pressure distribution along the fault. In low-porous carbonate rocks with high stiffness, all deformation tends to be accommodated in the fault zone. Fracture flow results in a local distribution of pore pressure, which causes early reactivation under critically stressed conditions. In contrast, porous carbonate rocks allow both the fault and matrix to accommodate deformation, resulting in a more uniform distribution of pore pressure along the fault.
- What are the implications of these findings for induced seismicity in geothermal carbonate reser-

voirs?
Induced seismicity appears to be a higher risk in a critically stressed fault zone with less porous carbonate rock that exhibits secondary permeability in the form of fractures. Additionally, the effect of juxtaposition depends on the pore pressure distribution along the fault in the member that allows matrix flow. This results in a critical pore pressure that tends towards the critical pore pressure in a porous reservoir.

References

Abd El-Aal, Ahmed K et al. (2021). “Carbonate strength classification based on depositional textures and fossil content of the Lower Eocene Drunka Formation, Assiut Area, central Egypt”. In: *Journal of Petroleum Science and Engineering* 207, p. 109061. ISSN: 0920-4105. DOI: https://doi.org/10.1016/j.petrol.2021.109061. URL: https://www.sciencedirect.com/science/article/pii/S092041052100718X.

Agosta, Fabrizio and DL Kirschner (2003). “Fluid conduits in carbonate-hosted seismogenic normal faults of central Italy”. In: *Journal of Geophysical Research: Solid Earth* 108.B4. DOI: https://doi.org/10.1029/2002JB002013.

Ahr, Wayne M (2011). *Geology of carbonate reservoirs: the identification, description and characterization of hydrocarbon reservoirs in carbonate rocks*. John Wiley & Sons.

Aki, Keiiti (1984). “Asperities, barriers, characteristic earthquakes and strong motion prediction”. In: *Journal of Geophysical Research: Solid Earth* 89.B7, pp. 5867–5872. DOI: https://doi.org/10.1029/JB089iB07p05867.

Archie, Gustave Erdman (1952). “Classification of carbonate reservoir rocks and petrophysical considerations”. In: *Aapg Bulletin* 36.2, pp. 278–298.

Baisch, S. and R. Vörös (Dec. 2018). “Earthquakes Near the Californie Geothermal Site: August 2015 – November 2018”. In: Report prepared for Californie Lipzig Gielen Geothermie BV.

— (Mar. 2019). *Seismic Hazard Assessment for the CLG-Geothermal System – Study Update March 2019*. Report.

Bastesen, Eivind and Alvar Braathen (2010). “Extensional faults in fine grained carbonates – analysis of fault core lithology and thickness–displacement relationships”. In: *Journal of Structural Geology* 32.11. Fault Zones, pp. 1609–1628. ISSN: 0191-8141. DOI: https://doi.org/10.1016/j.jsg.2010.09.008.

Bloemendal, Martin, Marc Jaxa-Rozen, and Theo Olsthoorn (2018). “Methods for planning of ATES systems”. In: *Applied Energy* 216, pp. 534–557. ISSN: 0306-2619. DOI: https://doi.org/10.1016/j.apenergy.2018.02.068. URL: https://www.sciencedirect.com/science/article/pii/S0306261918301958.

Bloemendal, Martin, Theo Olsthoorn, and Frans van de Ven (2015). “Combining climatic and geohydrological preconditions as a method to determine world potential for aquifer thermal energy storage”. In: *Science of the Total Environment* 538, pp. 621–633. DOI: https://doi.org/10.1016/j.scitotenv.2015.07.084.

Bonté, Damien, J-D Van Wees, and JM Verweij (2012). “Subsurface temperature of the onshore Netherlands: new temperature dataset and modelling”. In: *Netherlands Journal of Geosciences* 91.4, pp. 491–515. DOI: DOI={10.1017/S0016774600000354}.

Bos, S and B Laenen (2017). “Development of the first deep geothermal doublet in the Campine Basin of Belgium”. In: *European Geologist* 43, pp. 16–20.

Boxem, T. et al. (2015). *Eindrapport Ultra-Diepe Geothermie in Nederland*. Final Report on Ultra-Deep Geothermal Energy in the Netherlands.

Breede, Katrin, Khatia Dzebisashvili, and Gioia Falcone (2015). “Overcoming challenges in the classification of deep geothermal potential”. In: *Geothermal Energy Science* 3.1, pp. 19–39. DOI: 10.5194/gtes-3-19-2015.

Broothaers, Matsen et al. (Dec. 2021). “Deep geothermal energy in the Lower Carboniferous carbonates of the Campine Basin, northern Belgium: An overview from the 1950?s to 2020”. In: *Zeitschrift der Deutschen Gesellschaft für Geowissenschaften* 172.3, pp. 211–225. DOI: 10.1127/zdgg/2021/0285. URL: http://dx.doi.org/10.1127/zdgg/2021/0285.

Brown, Stephen R (1987). “A note on the description of surface roughness using fractal dimension”. In: *Geophysical Research Letters* 14.11, pp. 1095–1098. DOI: https://doi.org/10.1029/GL014i011p01095.

Buijze, Loes et al. (2019). “Review of induced seismicity in geothermal systems worldwide and implications for geothermal systems in the Netherlands”. In: *Netherlands Journal of Geosciences* 98, e13. DOI: 10.1017/njg.2019.6.

Bussolotto, Maura et al. (2007). “Deformation features within an active normal fault zone in carbonate rocks: The Gubbio fault (Central Apennines, Italy)”. In: *Journal of Structural Geology* 29.12, pp. 2017–2037. ISSN: 0191-8141. DOI: https://doi.org/10.1016/j.jsg.2007.07.014.

Byerlee, J. (1978). “Friction of rocks”. In: *Pure and Applied Geophysics* 116, pp. 615–626. DOI: https://doi.org/10.1007/BF00876528.

Caine, Jonathan Saul, James P Evans, and Craig B Forster (1996). “Fault zone architecture and permeability structure”. In: *Geology* 24.11, pp. 1025–1028. DOI: https://doi.org/10.1130/0091-7613(1996)024<1025:FZAAPS>2.3.CO;2.

Candela, Thibault et al. (2012). “Roughness of fault surfaces over nine decades of length scales”. In: *Journal of Geophysical Research: Solid Earth* 117.B8. DOI: https://doi.org/10.1029/2011JB009041.

Cesca, Simone et al. (2021). “Seismicity at the Castor gas reservoir driven by pore pressure diffusion and asperities loading”. In: *Nature Communications* 12.1, p. 4783. DOI: https://doi.org/10.1038/s41467-021-24949-1.

Childs, Conrad et al. (2009). “A geometric model of fault zone and fault rock thickness variations”. In: *Journal of Structural Geology* 31.2, pp. 117–127. DOI: https://doi.org/10.1016/j.jsg.2008.08.009.

Chilingar, George V, Harold J Bissell, and Rhodes W Fairbridge (2011). *Carbonate rocks*. Elsevier.

Choquette, Philip W and Lloyd C Pray (1970). “Geologic nomenclature and classification of porosity in sedimentary carbonates”. In: *AAPG bulletin* 54.2, pp. 207–250.

Cilona, Antonino et al. (2012). “Deformation bands in porous carbonate grainstones: Field and laboratory observations”. In: *Journal of Structural Geology* 45, pp. 137–157. DOI: https://doi.org/10.1016/j.jsg.2012.04.012.

Cook, Peter J (2017). “CCS research development and deployment in a clean energy future: Lessons from Australia over the past two decades”. In: *Engineering* 3.4, pp. 477–484. DOI: https://doi.org/10.1016/J.ENG.2017.04.014.

Coulomb, Charles Augustin (1776). *Essai sur une application des règles de maximis & minimis à quelques problèmes de statique à l’architecture*. De l’Imprimerie Royale.

Delle Piane, Claudio et al. (2017). “Carbonate hosted fault rocks: A review of structural and microstructural characteristic with implications for seismicity in the upper crust”. In: *Journal of Structural Geology* 103, pp. 17–36. ISSN: 0191-8141. DOI: https://doi.org/10.1016/j.jsg.2017.09.003. URL: https://www.sciencedirect.com/science/article/pii/S0191814117301748.

Di Toro, Giulio et al. (2011). “Fault lubrication during earthquakes”. In: *Nature* 471.7339, pp. 494–498. DOI: https://doi:10.1038/nature09838.

Diehl, Tobias et al. (2017). “The induced earthquake sequence related to the St. Gallen deep geothermal project (Switzerland): Fault reactivation and fluid interactions imaged by microseismicity”. In: *Journal of Geophysical Research: Solid Earth* 122.9, pp. 7272–7290. DOI: https://doi.org/10.1002/2017JB014473.

Dieterich, James H (1979). “Modeling of rock friction: 1. Experimental results and constitutive equations”. In: *Journal of Geophysical Research: Solid Earth* 84.B5, pp. 2161–2168. DOI: https://doi.org/10.1029/JB084iB05p02161.

Dunham, Robert J (1962). “Classification of carbonate rocks according to depositional textures”. In.

Dussel, Michael et al. (2018). “Characterization of a Deep Fault Zone in Upper Jurassic Carbonates of the Northern Alpine Foreland Basin for Geotherma Production (South Germany)”. In: *Proceedings of the 43rd Workshop on Geothermal Reservoir Engineering*.

Ellsworth, William L. (2013). “Injection-Induced Earthquakes”. In: *Science* 341.6142, p. 1225942. DOI: 10.1126/science.1225942. URL: https://www.science.org/doi/abs/10.1126/science.1225942.

Energie Beheer Nederland (2025). *Energie in Cijfers*. Accessed: April 15, 2025. URL: https://www.ebn.nl/energie-in-cijfers.

Faulkner, DR et al. (2010). “A review of recent developments concerning the structure, mechanics and fluid flow properties of fault zones”. In: *Journal of Structural Geology* 32.11, pp. 1557–1575. DOI: https://doi.org/10.1016/j.jsg.2010.06.009.

Fjaer, Eirik (2010). *Petroleum Related Rock Geomechanics*. 1st. Oxford, UK: Elsevier. ISBN: 978-0-08-045751-4.

Gadelmawla, E.S. et al. (2002). “Roughness parameters”. In: *Journal of Materials Processing Technology* 123.1, pp. 133–145. ISSN: 0924-0136. DOI: https://doi.org/10.1016/S0924-0136(02)00060-2.

Gardiner, Nicholas J et al. (2023). “Geosciences and the energy transition”. In: *Earth Science, Systems and Society* 3.1, p. 10072. DOI: doi:10.3389/esss.2023.10072.

Hart, David J and Herbert F Wang (1995). “Laboratory measurements of a complete set of poroelastic moduli for Berea sandstone and Indiana limestone”. In: *Journal of Geophysical Research: Solid Earth* 100.B9, pp. 17741–17751. DOI: https://doi.org/10.1029/95JB01242.

Hoek, E. and C.D. Martin (2014). “Fracture initiation and propagation in intact rock – A review”. In: *Journal of Rock Mechanics and Geotechnical Engineering* 6.4, pp. 287–300. ISSN: 1674-7755. DOI: https://doi.org/10.1016/j.jrmge.2014.06.001.

Hoek, Evert and James A. Franklin (1968). “The Hoek Cell: A New Apparatus for Measuring the Strength of Rock Materials Under Controlled Stress Conditions”. In: *Geotechnique* 18.1, pp. 55–67. DOI: 10.1680/geot.1968.18.1.55.

Hurst, Harold Edwin (1951). “Long-term storage capacity of reservoirs”. In: *Transactions of the American society of civil engineers* 116.1, pp. 770–799. DOI: https://doi.org/10.1061/TACEAT.0006518.

International Energy Agency (2024). *Global Energy and Climate Model*. Licence: CC BY 4.0. Paris. URL: https://www.iea.org/reports/global-energy-and-climate-model.

International Energy Agency (IEA) (2025). *Energy system of The Netherlands, Germany, France, Belgium and the UK*. Accessed: 29 April 2025. URL: https:/https://www.iea.org/regions/europe.

Jaeger, John Conrad, Neville GW Cook, and Robert Zimmerman (2007). *Fundamentals of Rock Mechanics*. 4th. Malden, MA: Blackwell Publishing. ISBN: 978-0632057597.

Ji, Yinlin, Hannes Hofmann, et al. (2022). “Laboratory experiments on fault behavior towards better understanding of injection-induced seismicity in geoenergy systems”. In: *Earth-Science Reviews* 226, p. 103916. DOI: https://doi.org/10.1016/j.earscirev.2021.103916.

Ji, Yinlin, Lei Wang, et al. (2022). “High-rate fluid injection reduces the nucleation length of laboratory earthquakes on critically stressed faults in granite”. In: *Geophysical Research Letters* 49.23, e2022GL100418. DOI: https://doi.org/10.1029/2022GL100418.

Ji, Yinlin, Li Zhuang, et al. (2020). “Cyclic Water Injection Potentially Mitigates Seismic Risks by Promoting Slow and Stable Slip of a Natural Fracture in Granite”. In: *Rock Mechanics and Rock Engineering* 54, pp. 5389–5405. DOI: 10.1007/s00603-021-02438-7. URL: https://doi.org/10.1007/s00603-021-02438-7.

Kortram, Jon-Danilo, Auke Barnhoorn, and Anne Pluymakers (2023). “Laboratory experiments on the effects of corrosion inhibitor on the mechanical properties of reservoir rock”. In: *Geothermal Energy* 11.1, p. 17. DOI: https://doi.org/10.1186/s40517-023-00257-3.

Labuz, Joseph F and Arno Zang (2014). “Mohr–Coulomb failure criterion”. In: *The ISRM Suggested Methods for Rock Characterization, Testing and Monitoring: 2007-2014*. Springer, pp. 227–231.

Li, Kai and Anne MH Pluymakers (2024). “Effects of thermal shocks on integrity of existing and newly-designed sealants for CCS applications”. In: *International Journal of Greenhouse Gas Control* 133, p. 104103. DOI: https://doi.org/10.1016/j.ijggc.2024.104103.

Lin, Tong et al. (2021). “Using characteristics of pressure-temperature induced permeability variation of typical carbonate rock to determine its performance as reservoir or cap rock”. In: *Journal of Natural Gas Geoscience* 6.1, pp. 1–12. ISSN: 2468-256X. DOI: https://doi.org/10.1016/j.jnggs.2020.11.004.

Lopez, Simon et al. (2010). “40 years of Dogger aquifer management in Ile-de-France, Paris Basin, France”. In: *Geothermics* 39.4, pp. 339–356. DOI: https://doi.org/10.1016/j.geothermics.2010.09.005.

Lucia, FJ (1983). “Petrophysical parameters estimated from visual descriptions of carbonate rocks: a field classification of carbonate pore space”. In: *Journal of petroleum technology* 35.03, pp. 629–637.

Mandelbrot, Benoit (1967). “How long is the coast of Britain? Statistical self-similarity and fractional dimension”. In: *science* 156.3775, pp. 636–638.

Mandelbrot, Benoit (1985). “Self-affine fractals and fractal dimension”. In: *Physica scripta* 32.4, p. 257. DOI: https://doi.org/10.1088/0031-8949/32/4/001.

Mandelbrot, Benoit B. and James R. Wallis (1969). “Robustness of the rescaled range R/S in the measurement of noncyclic long run statistical dependence”. In: *Water Resources Research* 5.5, pp. 967–988. DOI: https://doi.org/10.1029/WR005i005p00967.

Masterplan (2018). *Masterplan Aardwarmte in Nederland - Een Brede Basis Voor Een Duurzame Warmtevoorziening*. Accessed: January 19, 2025. URL: https://www.geothermie.nl/images/Onderzoeken-en-rapporten/20180529-Masterplan-Aardwarmte-in-Nederland.pdf.

Micarelli, L., A. Benedicto, and C.A.J. Wibberley (2006). “Structural evolution and permeability of normal fault zones in highly porous carbonate rocks”. In: *Journal of Structural Geology* 28.7, pp. 1214–1227. ISSN: 0191-8141. DOI: https://doi.org/10.1016/j.jsg.2006.03.036. URL: https://www.sciencedirect.com/science/article/pii/S0191814106000873.

Ministerie van Klimaat en Groene Groei (2023). *Delfstoffen en Aardwarmte in Nederland: Jaarverslag 2023*. Accessed: April 15, 2025. URL: https://www.nlog.nl/sites/default/files/2024-09/Jaarverslag%202023%20-%20Delfstoffen%20en%20aardwarmte%20in%20Nederland.pdf.pdf.

Mohr, O. (1900). “Welche Umstände bedingen die Elastizitätsgrenze und den Bruch eines Materials?” In: *Zeitschrift des Vereins Deutscher Ingenieure* 44, pp. 1524–1530.

Montanari, D et al. (2017). “Geothermal resources within carbonate reservoirs in western Sicily (Italy): A review”. In: *Earth-Science Reviews* 169, pp. 180–201. DOI: https://doi.org/10.1016/j.earscirev.2017.04.016.

Moore, Clyde H. and William J. Wade (2013). “Chapter 4 - The Nature and Classification of Carbonate Porosity”. In: *Carbonate Reservoirs*. Ed. by Clyde H. Moore and William J. Wade. Vol. 67. Developments in Sedimentology. Elsevier, pp. 51–65. DOI: https://doi.org/10.1016/B978-0-444-53831-4.00004-5. URL: https://www.sciencedirect.com/science/article/pii/B9780444538314000045.

Mozafari, Mahtab et al. (2019). *Facies Analysis and Diagenetic Evolution of the Dinantian Carbonates in the Dutch Subsurface*. Technical Report. Report commissioned by the Ministry of Economic Affairs and Climate Policy (The Netherlands). Utrecht, The Netherlands: SCAN Program, Energie Beheer Nederland (EBN). URL: https://www.nlog.nl/en/scan-results.

Okubo, Paul G and James H Dieterich (1984). “Effects of physical fault properties on frictional instabilities produced on simulated faults”. In: *Journal of Geophysical Research: Solid Earth* 89.B7, pp. 5817–5827. DOI: https://doi.org/10.1029/JB089iB07p05817.

Peacock, D.C.P (2002). “Propagation, interaction and linkage in normal fault systems”. In: *Earth-Science Reviews* 58.1, pp. 121–142. ISSN: 0012-8252. DOI: https://doi.org/10.1016/S0012-8252(01)00085-X.

Peacock, DCP and DJ Sanderson (1992). “Effects of layering and anisotropy on fault geometry”. In: *Journal of the Geological Society* 149.5, pp. 793–802. DOI: https://doi.org/10.1144/gsjgs.149.5.0793.

Perras, Matthew A and Mark S Diederichs (2011). “The importance of classification for carbonates and mudrocks in engineering”. In: *Proceedings of the 2011 Pan-Am Canadian Geotechnical Conference, Toronto*.

Power, William L, Terry E Tullis, and John D Weeks (1988). “Roughness and wear during brittle faulting”. In: *Journal of Geophysical Research: Solid Earth* 93.B12, pp. 15268–15278. DOI: https://doi.org/10.1029/JB093iB12p15268.

Přikryl, R (2001). “Some microstructural aspects of strength variation in rocks”. In: *International Journal of Rock Mechanics and Mining Sciences* 38.5, pp. 671–682. DOI: https://doi.org/10.1016/S1365-1609(01)00031-4.

Quinton, Page (2025). *Dunham classification for carbonate rocks. Diagram after Dunham, 1962: Classification of carbonate rocks according to depositional textures*. Accessed: 2025-01-20. URL: https://commons.wikimedia.org/wiki/File:Example_Figure.jpg.

Reijmer, John JG et al. (2017). “Seismic stratigraphy of Dinantian carbonates in the southern Netherlands and northern Belgium”. In: *Netherlands Journal of Geosciences* 96.4, pp. 353–379. DOI: https://doi:10.1017/njg.2017.33.

Rijksoverheid (2019). *Klimaatakkoord*. Accessed: January 3, 2025. URL: https://www.rijksoverheid.nl/onderwerpen/duurzame-energie/aardwarmte.

Rotevatn, Atle et al. (2016). “Sequential growth of deformation bands in carbonate grainstones in the hangingwall of an active growth fault: Implications for deformation mechanisms in different tectonic regimes”. In: *Journal of Structural Geology* 90, pp. 27–47. ISSN: 0191-8141. DOI: https://doi.org/10.1016/j.jsg.2016.07.003.

Ruina, Andy (1983). “Slip instability and state variable friction laws”. In: *Journal of Geophysical Research: Solid Earth* 88.B12, pp. 10359–10370. DOI: https://doi.org/10.1029/JB088iB12p10359.

Sagy, Amir, Emily E Brodsky, and Gary J Axen (2007). “Evolution of fault-surface roughness with slip”. In: *Geology* 35.3, pp. 283–286. DOI: https://doi.org/10.1130/G23235A.1.

Seithel, Robin et al. (2019). “Probability of fault reactivation in the Bavarian Molasse Basin”. In: *Geothermics* 82, pp. 81–90. DOI: https://doi.org/10.1016/j.geothermics.2019.06.004.

The Engineering Toolbox (2025). *Young’s Modulus of Elasticity - Values for Common Materials*. Accessed: 2025-06-16. URL: https://www.engineeringtoolbox.com/young-modulus-d_417.html.

Torabi, Anita, TSS Ellingsen, et al. (2019). “Fault zone architecture and its scaling laws: where does the damage zone start and stop?” In: *Geological Society* 496, pp. 99–124. DOI: https://doi.org/10.1144/SP496-2018-151.

Torabi, Anita, Magnus Ueland Johannessen, and Tor Saltnes Skram Ellingsen (2019). “Fault core thickness: Insights from siliciclastic and carbonate rocks”. In: *Geofluids* 2019.1, p. 2918673.

UNFCCC (2015). *Paris Agreement*. Accessed: January 3, 2025. URL: https://unfccc.int/process-and-meetings/the-paris-agreement/the-paris-agreement.

Vardon, Phil et al. (2025). *Producing geothermal energy in the Delft Subsurface Urban Energy Lab*. Accessed: January 19, 2025. URL: https://www.innovationnewsnetwork.com/producing-geothermal-energy-delft-subsurface-urban-energy-lab/32725/.

Veltmeijer, A et al. (2024). “Precursory signals to injection induced fault reactivation in the laboratory using active ultrasonic monitoring methods”. In: *Journal of Geophysical Research: Solid Earth* 129.2, e2023JB028505. DOI: https://doi.org/10.1029/2023JB028505.

Walton, G et al. (2017). “Post-yield strength and dilatancy evolution across the brittle–ductile transition in Indiana limestone”. In: *Rock Mechanics and Rock Engineering* 50, pp. 1691–1710. DOI: https://doi.org/10.1007/s00603-017-1195-1.

Wibberley, Christopher A. J., Graham Yielding, and Giulio Di Toro (2008). “Recent advances in the understanding of fault zone internal structure: a review”. In: *Geological Society, London, Special Publications* 299.1, pp. 5–33. DOI: https://doi.org/10.1144/SP299.2.

Ye, Zhi and Ahmad Ghassemi (2018). “Injection-induced shear slip and permeability enhancement in granite fractures”. In: *Journal of Geophysical Research: Solid Earth* 123.10, pp. 9009–9032. DOI: 10.1029/2018JB016045. URL: https://doi.org/10.1029/2018JB016045.

Zhu, Wei, Patrick Baud, and Teng-fong Wong (2010). “Micromechanics of cataclastic pore collapse in limestone”. In: *Journal of Geophysical Research: Solid Earth* 115.B4. DOI: https://doi.org/10.1029/2009JB006610.

A

Appendix

A.1. Calibration of 500 kN apparatus setup

During the experiments performed with the 500 kN apparatus, we measured the total axial displacement using LVDTs. These measurements include not only the deformation of the sample itself but also the deformation of all machine components. Therefore, we needed to correct the measured axial strain in the UCS and triaxial configurations at a confining pressure of 35 MPa.

To correct the axial strain, we needed to do a calibration test using a steel cylinder with a length of 59.33 mm and a diameter of 30.11 mm. We took a value of 200 GPa for the Young's modulus of the steel (The Engineering Toolbox, 2025). Since we know the Young's modulus of steel, we can calculate the elastic strain as a function of axial stress with Hooke's Law as described in Equation A.1:

$$\epsilon_{\text{steel}} = \frac{\sigma}{E_{\text{steel}}} \tag{A.1}$$

Now that we know the actual elastic strain of steel as a function of axial stress, we can correct the measurement of the experiment that contains both the machine and steel. We can do this as described in Equation A.2

$$\epsilon_{machine} = \epsilon_{machine+steel} - \epsilon_{steel} \tag{A.2}$$

For the linear part of the stress-strain curve of the machine, we can determine the Young's modulus of the machine, which can be used to correct all measurements of experiments. Therefore, we can describe the axial strain of the sample as in Equation A.3

$$\epsilon_{sample} = \epsilon_{experiment} - \frac{\sigma}{E_{machine}} \tag{A.3}$$

In Figure A.1 & Figure A.2 we visualise the results of the correction test. Here, we see that the steel sample after correction has almost a Young's modulus of 200 GPa.

A.1.1. Setup correction for UCS

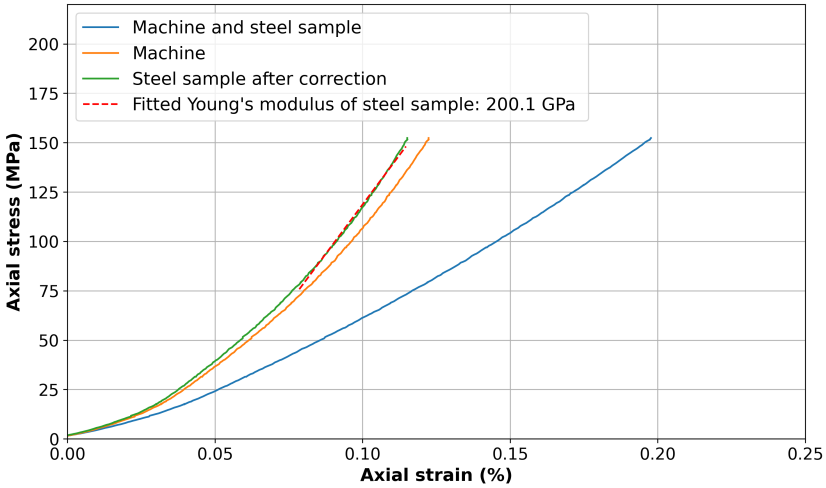

Figure A.1: Setup correction for the UCS experiments

A.1.2. Setup correction for Triaxial experiments at 35 MPa

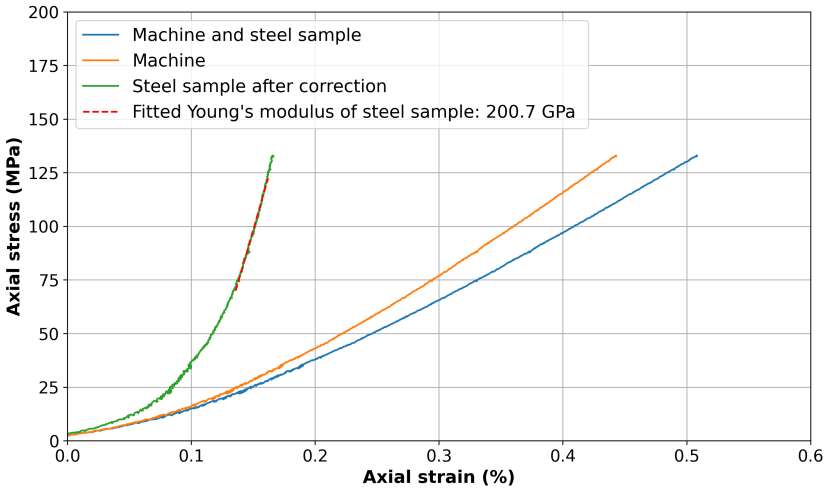

Figure A.2: Setup correction for the triaxial experiments at 35 MPa of confining stress